# Evaluation of higher-order time-domain perturbation theory of photon diffusion on breast-equivalent phantoms and optical mammograms

D. Grosenick,[1] A. Kummrow,[1] R. Macdonald,[1] P. M. Schlag,[2] and H. Rinneberg[1]

[1]*Physikalisch-Technische Bundesanstalt, Abbestrasse 2-12, 10587 Berlin, Germany*
[2]*Robert-Rössle-Hospital, Charité, University Medicine Berlin, Lindenberger Weg 80, 13125 Berlin, Germany*
(Received 22 November 2006; revised manuscript received 21 September 2007; published 13 December 2007)

Time-domain perturbation theory of photon diffusion up to third order was evaluated for its accuracy in deducing optical properties of breast tumors using simulated and physical phantoms and by analyzing 141 projection mammograms of 87 patients with histology-validated tumors that had been recorded by scanning time-domain optical mammography. The slightly compressed breast was modeled as (partially) homogeneous diffusely scattering infinite slab containing a scattering and absorbing spherical heterogeneity representing the tumor. Photon flux densities were calculated from densities of transmitted photons, assuming extended boundary conditions. Explicit formulas are provided for second-order changes in transmitted photon density due to the presence of absorbers or scatterers. The results on phantoms obtained by perturbation theory carried up to third order were compared with measured temporal point spread functions, with numerical finite-element method (FEM) simulations of transmitted photon flux density, with results obtained from the diffraction of diffuse photon density waves, and from Padé approximants. The breakdown of first-, second-, and third-order perturbation theory is discussed for absorbers and a general expression was derived for the convergence of the Born series in this case. Taking tumor optical properties derived by the diffraction model as reference we conclude that estimates of tumor absorption coefficients by perturbation theory agree with reference values within ±25% in only 65% (first order), 66% (second order), and 77% (third order) of all mammograms analyzed. In the remaining cases tumor absorption is generally underestimated due to the breakdown of perturbation theory. On average the empirical Padé approximants yield tumor absorption coefficients similar to third-order perturbation theory, yet at noticeable lower computational efforts.

## I. INTRODUCTION

Optical mammography [1–8] aims at the detection of breast cancer and, in particular, at the characterization of tumors [9–12] by diffuse optical spectroscopy to aid diagnosis and therapy control. From diffusely transmitted or reflected near infrared light absorption and scattering properties of breast tissue including benign and malignant lesions may be reconstructed provided tomographic arrangements of sources and detectors are used, i.e., the diffusely transmitted light is recorded at a sufficient number of projection angles. Both linear and nonlinear forward models, e.g., numerical finite-element (FEM) solutions of the diffusion equation, are employed to solve the ill-posed inverse problem. Paraxial scanning mammographs, on the other hand, directly provide shadowgrams of the breast slightly compressed between two glass plates that do not require the solution of the ill-posed problem. Because of poor angular sampling, however, little information on the precise location of the tumor along the compression direction and on its volume is obtained from such measurements in general. Therefore, when analyzing paraxial mammograms recorded in time domain or frequency domain for tumor optical properties, prior knowledge on the location and size of the tumor, if available, should be included in the analysis, otherwise tumor size and its depth location have to be assumed. Subsequently, tumor optical properties are derived from measured data by fitting the flux density of transmitted photons predicted by forward models based on the diffusion approximation. Early approaches to generate optical mammograms displaying tissue optical properties from coaxial scanning data were based on a homogeneous infinite slab as a simplified model for a tumor-bearing, compressed breast [13]. However, this model yields only average optical properties, with rather uncertain information on the absorption and scattering properties of lesions. Consequently, more realistic models were applied representing tumor-bearing breasts as a partially homogeneous slab containing one or several heterogeneities with optical properties differing from those of the surrounding background medium. Linear perturbation theory, i.e., Born approximation of the optical diffusion equation, was used to derive tumor optical properties and to generate optical projection mammograms displaying tissue optical properties [14–20] at improved contrast. However, linear perturbation theory might fail to precisely derive the absorption coefficients of strongly absorbing heterogeneities or inclusions of considerable size, a situation often encountered with tumors detected by optical mammography. Furthermore, linear perturbation theory might not be applicable when several inhomogeneities are present as pointed out by Arridge *et al.* [21]. Therefore, several attempts were made to develop forward models beyond the linear approximation. Ostermeyer and Jacques [17] developed higher-order perturbation theory in frequency domain accounting for the presence of absorbing and scattering inhomogeneities embedded in an infinite medium. For this purpose these authors introduced virtual source strengths being either proportional to the (unknown) fluence or to its gradient and solved for the perturbed fluence by numerical iteration. The results obtained in this way for embedded, homogeneous spherical absorbers and scatterers were compared

with the solution of the diffusion equation based on the diffraction of diffuse photon density waves (DPDW) by a spherical heterogeneity. The perturbation of the fluence exhibits a monopole pattern in case of an absorber, whereas a scatterer produces predominantly a dipolar pattern corresponding to a surface-induced backscattering. A rather accurate, yet empirical nonlinear approach based on the method of Padé approximants was introduced by Torricelli *et al.* [22,23]. As discussed below, the Padé expression works generally well for pure absorbers, i.e., it never yields negative values for the time-resolved transmittance, a problem encountered with linear perturbation theory for sufficiently strong absorbers. However, the empirical approach may fail for inhomogeneities with lower scattering or absorption compared to the surrounding medium.

Recently, general expressions for transmitted time-domain photon flux densities based on second- and higher-order perturbation theory were reported by Wassermann [24]. The present paper critically assesses second- and third-order time-domain perturbation theory on breast-equivalent phantoms for deriving optical properties of tumor-simulating heterogeneities. Both simulated photon flux densities obtained from FEM calculations on virtual (numerical) phantoms and measured temporal point spread (TPS) functions, i.e., distributions of times of flight of photons, using physical phantoms were analyzed in this way. The results obtained are compared either with known optical properties of the spherical heterogeneity or with those derived using the diffraction of DPDW as exact forward model [10,13,25–28]. For this purpose, a partially homogeneous infinite slab carrying a (homogeneous) spherical heterogeneity as absorber was selected to simulate a tumor-bearing compressed breast, although perturbation theory allows us to analyze arbitrary shapes of heterogeneities as well. Whereas virtual and physical phantom studies allow us to assess limitations of first- and higher-order perturbation theory including Padé approximants, only limited information can be obtained in this way whether such models are suited to analyze *in vivo* data for tumor optical properties. The extent to which deficiencies of the various forward models affect the analysis of optical mammograms depends on the distributions of size and optical properties of tumors that are generally detected by optical mammography. Therefore we reanalyzed about 140 optical mammograms of tumor-bearing breasts that had been recorded during a previous clinical trial on optical mammography [6] and compared the results on 87 tumors obtained from perturbation theory with their optical properties that had been derived previously from the same data using the diffraction of DPDW as forward model [29]. In this way we estimated the extent to which perturbation theory and Padé approximants can be expected to yield meaningful optical properties of tumors when used as forward models in the analysis of *in vivo* optical data.

The paper is organized as follows. In Sec. II we outline our method for calculating second- and higher-order contributions to perturbed transmittance, being more efficient than using the formulas of Wassermann [24]. In addition we briefly compare our approach to solve for the perturbed photon density with the method of Ostermeyer and Jacques [17]. Section III deals with numerical forward simulations using perturbation theory up to third order, including Padé approximants, and with the analysis of simulated FEM data for the optical properties of the heterogeneity. Section IV describes phantom measurements including the reconstruction of optical properties of spherical heterogeneities from measured TPS functions and from simulated photon flux densities applying perturbation theory, Padé approximants, and diffraction of DPDW, discussing the limitations of the various forward models used. In Sec. V we reanalyze the majority of our optical mammograms of tumor-bearing breasts for tumor optical properties using perturbation theory up to third order and Padé approximants and compare the tumor optical properties obtained from perturbation theory with our diffraction results published previously [29]. A brief discussion (Sec. VI) summarizes the results obtained in this paper and their impact on data analysis of time-domain optical mammograms for tumor optical properties.

## II. THEORY

Breast tissue is highly scattering but weakly absorbing in the near infrared spectral range and propagation of red or near infrared light in this type of tissue can be described by the optical diffusion equation [30]. Here we consider a tumor-bearing breast compressed between two parallel glass plates as partially homogeneous infinite slab of thickness $d$ with a spherical heterogeneity of volume $V = (4\pi/3)R_{imp}^3$ with sharp boundaries. The absorption coefficient $\mu_{a0}$ and the reduced scattering coefficient $\mu'_{s0}$ denote the background optical properties of the homogeneous part of the slab and the absorption coefficient $\mu_a = \mu_{a0} + \delta\mu_a$ and reduced scattering coefficient $\mu'_s = \mu'_{s0} + \delta\mu'_s$ of the heterogeneity represent perturbations. The dynamic diffusion coefficient of the background medium is given by $D_0 = 1/(3\mu'_{s0})$ and, likewise, that of the heterogeneity by $D = D_0 + \delta D = 1/(3\mu'_s)$ [31,32]. In this case the Born series is a power series in changes $\delta\mu_a$ of the absorption coefficient and changes $\delta D$ of the diffusion coefficient. In this section, the corrections to time-resolved photon density up to second order of this series are given and the convergence of the Born series for pure absorbers is discussed more generally on the expression for the corrections of order $N$.

### A. Corrections to time-resolved photon density up to second order

The total photon density $\phi(\vec{r}, t)$ is expressed as the sum of the photon density $\phi_0(\vec{r}, t)$ of the homogeneous slab and the perturbation $\delta\phi(\vec{r}, t)$ due to an absorbing and scattering heterogeneity

$$\phi(\vec{r}, t) = \phi_0(\vec{r}, t) + \delta\phi(\vec{r}, t), \tag{1}$$

where

$$\delta\phi(\vec{r}, t) = -\delta\mu_a \int_V dV_p \int_0^t dt_p G_{slab}(\vec{r}, t; \vec{r}_p, t_p) \phi(\vec{r}_p, t_p)$$

$$- \delta D \int_V dV_p \int_0^t dt_p \boldsymbol{\nabla}_p G_{slab}(\vec{r}, t; \vec{r}_p, t_p) \cdot \boldsymbol{\nabla}_p \phi(\vec{r}_p, t_p). \tag{2}$$

The Green's function $G_{slab}(\vec{r}, t; \vec{r}', t')$ of an infinite homoge-

neous slab entering Eq. (2) can be derived from the one for an infinite medium by introducing positively and negatively counted mirror photon sources and sinks [14,33]. The Green's function $G_{slab}(\vec{r},t;\vec{r}_0,0)$ describes the fluence in a homogeneous slab after excitation by a temporal and spatial $\delta$ pulse at position $\vec{r}_0=(0,0,z_0)$ with $z_0=1/\mu'_{s0}$. Following the perturbational approach outlined by Arridge [14,21], first and higher corrections can be written as

$$\delta\phi(\vec{r},t) = \delta\phi_a^{(1)}(\vec{r},t) + \delta\phi_D^{(1)}(\vec{r},t) + \delta\phi_{aa}^{(2)}(\vec{r},t) + \delta\phi_{aD}^{(2)}(\vec{r},t)$$
$$+ \delta\phi_{Da}^{(2)}(\vec{r},t) + \delta\phi_{DD}^{(2)}(\vec{r},t) + \delta\phi_{aaa}^{(3)}(\vec{r},t) + \cdots , \quad (3)$$

where $\delta\phi_a^{(1)}(\vec{r},t)$ is the term proportional to $\delta\mu_a$, $\delta\phi_D^{(1)}(\vec{r},t) \sim \delta D$, $\delta\phi_{aD}^{(2)}(\vec{r},t) \sim \delta\mu_a\delta D$, and so on. At the detector, the change in transmission, i.e., the change in the transmitted photon flux density along the outward pointing normal (positive $z$ axis), is calculated from the changes in photon density by

$$\delta T(\vec{r}_{det},t) = -vD_0\partial[\delta\phi(x_{det},y_{det},z,t)]/\partial z|_{z=d}, \quad (4)$$

where $\vec{r}_{det}=(x_{det},y_{det},d)$ denotes the position of the detector and $v$ the speed of light in the medium. For the slab geometry, extended boundary conditions are usually invoked to account for refractive index changes between tissue and the surrounding medium [34]. In this model the photon density falls to zero at virtual boundaries located at $z=-z_e$ and $z=d+z_e$. Since the distance $z_e$ is rather small, transmission changes can conveniently be calculated from

$$\delta T(\vec{r}_{det},t) = vD_0\delta\phi(\vec{r}_{det},t)/z_e. \quad (5)$$

This approach is numerically more efficient than to use Eq. (4) since explicit formulas for contributions to the transmitted photon flux density are substantially more complicated, obtained by differentiation of the corresponding contributions to the transmitted photon density.

Assuming $\phi_0(\vec{r},t)=G_{slab}(\vec{r},t;\vec{r}_0,0)/v$ without loss of generality the various changes in photon density corresponding to different orders of perturbation theory can thus be expressed as the sum over mirror images, yielding up to second order

$$\delta\phi_a^{(1)}(\vec{r}_{det},t) = \sum_{n,k=-\infty}^{\infty} \sum_{\alpha,\beta=0,1} (-1)^{\alpha+\beta} I_{n,k_{abs}}^{\alpha\beta^{(1)}}(\vec{r}_{det},t)$$
$$= [z_e/(vD_0)]\delta\mu_a f_a^{(1)}(\vec{r}_{det},t), \quad (6)$$

$$\delta\phi_D^{(1)}(\vec{r}_{det},t) = \sum_{n,k=-\infty}^{\infty} \sum_{\alpha,\beta=0,1} (-1)^{\alpha+\beta} I_{n,k_{scat}}^{\alpha\beta^{(1)}}(\vec{r}_{det},t)$$
$$= [z_e/(vD_0)]\delta D f_D^{(1)}(\vec{r}_{det},t), \quad (7)$$

$$\delta\phi_{aa}^{(2)}(\vec{r}_{det},t) = \sum_{m,n,k=-\infty}^{\infty} \sum_{\alpha,\beta,\gamma=0,1} (-1)^{\alpha+\beta+\gamma} I_{m,n,k_{abs-abs}}^{\alpha\beta\gamma^{(2)}}(\vec{r}_{det},t)$$
$$= [z_e/(vD_0)](\delta\mu_a)^2 f_{aa}^{(2)}(\vec{r}_{det},t), \quad (8)$$

TABLE I. Notations of distances, vectors, and their dot products.

| Second order | Higher order |
|---|---|
| $\vec{r}_{qk}^{\gamma}=\vec{r}_q-\vec{R}_{0k}^{\gamma}$ | $\vec{r}_{p,m_p}^{\pm}=\vec{r}_{p+1}-\vec{R}_{p,m_p}^{\pm}$ |
| $\vec{r}_{pn}^{\beta}=\vec{r}_p-\vec{R}_{qn}^{\beta}$ | with $p=0,\ldots N$; $m_p=-\infty,\ldots,\infty$ |
| $\vec{r}_m^{\alpha}=\vec{r}_{det}-\vec{R}_{pm}^{\alpha}$ | $\vec{r}_{N+1}=\vec{r}_{det}$ |
| | |
| $\vec{R}_{0k}^+=\vec{r}_0+2k(d+2z_e)\vec{e}_z$ | $\vec{R}_{p,m_p}^+=\vec{r}_p+2m_p(d+2z_e)\vec{e}_z$ |
| $\vec{R}_{qn}^+=\vec{r}_q+2n(d+2z_e)\vec{e}_z$ | |
| $\vec{R}_{pm}^+=\vec{r}_p+2m(d+2z_e)\vec{e}_z$ | |
| $\vec{R}_{0k}^-=\vec{r}_0+2[k(d+2z_e)-z_e-z_0]\vec{e}_z$ | $\vec{R}_{p,m_p}^-=\vec{r}_p+2[m_p(d+2z_e)-z_e-z_p]\vec{e}_z$ |
| $\vec{R}_{qn}^-=\vec{r}_q+2[n(d+2z_e)-z_e-z_q]\vec{e}_z$ | |
| $\vec{R}_{pm}^-=\vec{r}_p+2[m(d+2z_e)-z_e-z_p]\vec{e}_z$ | |
| | |
| $\vec{r}_m^{*\alpha}=\{x_m,y_m,(-1)^{\alpha}z_m^{\alpha}\}$ | note that in first order |
| $\vec{r}_{pn}^{*\beta}=\{x_{pn},y_{pn},(-1)^{\beta}z_{pn}^{\beta}\}$ | $p=1\Leftrightarrow p$ |
| $\vec{r}_{qk}^{**\gamma}=\{x_{qk},y_{qk},(-1)^{\beta}z_{qk}^{\gamma}\}$ | $m_0,m_1\Leftrightarrow k,n$ |
| $\vec{r}_{pq}^{**}=\vec{r}_{pn}^{*\beta}\cdot\vec{r}_{qk}^{\gamma}$ | $\alpha_0,\alpha_1\Leftrightarrow\beta,\alpha$ |
| | |
| $\vec{r}_{pm}^*=\vec{r}_{pn}^{\beta}\cdot\vec{r}_m^{*\alpha}$ | in second order |
| $\vec{r}_{qm}^{***}=\vec{r}_m^{*\alpha}\cdot\vec{r}_{qk}^{**\gamma}$ | $p=1, p=2\Leftrightarrow q,p$ |
| $r_{pq}^+=r_{pn}^{\beta}+r_{qk}^{\gamma}$ | $m_0,m_1,m_2\Leftrightarrow k,n,m$ |
| $r_{pqm}=r_{pq}^++r_m^{\alpha}$ | $\alpha_0,\alpha_1,\alpha_2\Leftrightarrow\gamma,\beta,\alpha$ |

$$\delta\phi_{aD}^{(2)}(\vec{r}_{det},t) = \sum_{m,n,k=-\infty}^{\infty} \sum_{\alpha,\beta,\gamma=0,1} (-1)^{\alpha+\beta+\gamma} I_{m,n,k_{abs-scat}}^{\alpha\beta\gamma^{(2)}}(\vec{r}_{det},t)$$
$$= [z_e/(vD_0)]\delta\mu_a\delta D f_{aD}^{(2)}(\vec{r}_{det},t), \quad (9)$$

$$\delta\phi_{Da}^{(2)}(\vec{r}_{det},t) = \sum_{m,n,k=-\infty}^{\infty} \sum_{\alpha,\beta,\gamma=0,1} (-1)^{\alpha+\beta+\gamma} I_{m,n,k_{scat-abs}}^{\alpha\beta\gamma^{(2)}}(\vec{r}_{det},t)$$
$$= [z_e/(vD_0)]\delta\mu_a\delta D f_{Da}^{(2)}(\vec{r}_{det},t), \quad (10)$$

$$\delta\phi_{DD}^{(2)}(\vec{r}_{det},t) = \sum_{m,n,k=-\infty}^{\infty} \sum_{\alpha,\beta,\gamma=0,1} (-1)^{\alpha+\beta+\gamma} I_{m,n,k_{scat-scat}}^{\alpha\beta\gamma^{(2)}}(\vec{r}_{det},t)$$
$$= [z_e/(vD_0)](\delta D)^2 f_{DD}^{(2)}(\vec{r}_{det},t). \quad (11)$$

Explicit formulas for the contributions $I^{(1,2)}(\vec{r}_{det},t)$ to the transmitted photon density are given in Appendix A (for notations, consistent with Ref. [24], see Table I). Second-order contributions [see Eqs. (A3)–(A6)] contain double volume integrals over positions $\vec{r}_p,\vec{r}_q$ located within the heterogeneity. It is shown in Appendix A that even in case both positions coincide ($\vec{r}_p=\vec{r}_q$) all volume integrals are integrable contrary to Ref. [24] where a logarithmic singularity was claimed to occur for the scattering-scattering contribution. The so-called shape functions $f_a^{(1)}, f_D^{(1)}, f_{aa}^{(2)},\ldots$ do not depend on $\delta\mu_a$ or $\delta D$ [16,20]. Approximate scaling relations for these shape functions are discussed in Appendix A that can be exploited when background optical properties are

changed, but the overall geometry is kept fixed.

We conclude this section by relating our results to the results obtained previously by other authors. In Ref. [24] the same approach was followed, yet explicit formulas for contributions to transmitted photon flux density were derived by analytical differentiation according to Eq. (4). We compared numerical results obtained by both methods and found them to agree. Furthermore, we relate our approach to the results of Ostermeyer and Jacques [17], who developed higher-order perturbation theory in frequency domain accounting for the presence of absorbing and scattering inhomogeneities embedded in an infinite medium. Equivalent to Eq. (2) the correction $\delta\phi(\vec{r},t)$ may be expressed in terms of virtual source densities $S_\phi^{virt}(\vec{r},t)$ and $S_J^{virt}(\vec{r},t)$ as

$$\delta\phi(\vec{r},t) = \int_V dV_p \int_0^t dt_p G_{slab}(\vec{r},t;\vec{r}_p,t_p) S_\phi^{virt}(\vec{r}_p,t_p)$$
$$+ \int_V dV_p \int_0^t dt_p G_{slab}(\vec{r},t;\vec{r}_p,t_p) S_J^{virt}(\vec{r}_p,t_p),$$
(12)

where

$$S_\phi^{virt}(\vec{r}_p,t_p) = \frac{\mu_{a0}\delta D - D_0\delta\mu_a}{D_0 + \delta D}\phi(\vec{r}_p,t_p)$$
$$+ \frac{\delta D}{v(D_0 + \delta D)}\frac{\partial\phi(\vec{r}_p,t_p)}{\partial t_p},$$
(13)

$$S_J^{virt}(\vec{r}_p,t_p) = \frac{D_0}{D_0 + \delta D}\boldsymbol{\nabla}_p\delta D(\vec{r}_p) \cdot \boldsymbol{\nabla}_p\phi(\vec{r}_p,t_p).$$
(14)

The virtual source densities $S_\phi^{virt}(\vec{r}_p,t_p)$ and $S_J^{virt}(\vec{r}_p,t_p)$ are proportional to the Fourier transforms of the corresponding source densities defined in frequency domain in Ref. [17]. However, since we use the expression $D=1/(3\mu_s')$ rather than $D=1/[3(\mu_a+\mu_s')]$ employed by Ostermeyer and Jacques, the virtual source density $S_J^{virt}(\vec{r}_p,t_p)$ given in Eq. (14) does not depend on $\delta\mu_a$.

### B. Convergence of Born series for pure absorbers

Aside from computational efforts to calculate higher-order corrections the question arises whether such contributions lead to substantial improvements or not. Therefore, it is desirable to estimate the conditions required for the Born series to converge. The general expression describing the $N^{th}$ order correction to the transmitted photon density for a pure absorber was reported by Wassermann [24] to be

$$\delta\phi_{abs}^{(N)}(\vec{r}_{det},t) = \sum_{m_0,\ldots,m_N=-\infty}^{\infty} \sum_{\alpha_0,\ldots,\alpha_N=0,1} (-1)^{\alpha_0+\cdots+\alpha_N} I_{m_0,\ldots,m_N}^{\alpha_0,\ldots,\alpha_N\,(N)},$$
(15)

$$I_{m_0,\ldots,m_N}^{\alpha_0,\ldots,\alpha_N\,(N)} = \frac{e^{-\mu_{a0}vt}}{(4\pi D_0 vt)^{3/2}}\left(\frac{-\delta\mu_a}{4\pi D_0}\right)^N \int_V \cdots \int_V \cdots \int_V \frac{\sum_{p=0}^N r_{p,m_p}^{\alpha_p}}{\prod_{p=0}^N r_{p,m_p}^{\alpha_p}}$$
$$\times\exp\left(-\frac{\left(\sum_{p=0}^N r_{p,m_p}^{\alpha_p}\right)^2}{4D_0 vt}\right)d^N V,$$
(16)

where $d^N V = dV_1 dV_2 \cdots dV_N$ and other notations used are defined in Table I. In Ref. [24] it was shown that the terms given in Eq. (16) are finite. However, in order to estimate convergence one has to prove that the terms vanish sufficiently fast with increasing order $N$. In Appendix B we provide upper limits for $|I_{m_0,\ldots,m_N}^{\alpha_0,\ldots,\alpha_N(N)}|$ and derive the following Cauchy criterion (Cauchy ratio test [35]) for the convergence of the Born series of a pure absorbing heterogeneity to be

$$C_{Cauchy} \equiv |\delta\mu_a|R_{imp}^2/(2D_0) < 1.$$
(17)

For values $\delta\mu_a=0.04$ cm$^{-1}$, $D_0=0.03$ cm, the critical value of $R_{imp}$ is 1.2 cm, which is typical for the size of tumors detected by optical mammography as discussed below. An increase of $\delta\mu_a$ by a factor of 2 reduces the acceptable size of the absorbing object to $R_{imp}=0.9$ cm to assure convergence of the Born series. The numerical and experimental results discussed below clearly indicate that application of perturbation theory does not make much sense when the criterion given in Eq. (17) is strongly violated.

## III. NUMERICAL FORWARD CALCULATIONS AND ANALYSIS OF SIMULATED DATA

For the evaluation of second- and third-order perturbation analysis we calculated time-resolved flux densities of transmitted photons using a virtual phantom that resembles the physical phantom used in the experiments discussed below. The virtual phantom was realized by forward calculations considering a diffusely scattering slab ($12\times12$ cm$^2$, thickness $d=6$ cm) with background optical properties $\mu_{a0}=0.045$ cm$^{-1}$ and $\mu_{s0}'=9.4$ cm$^{-1}$, close to experimental values. Spheres of various radii $R_{imp}=0.5\ldots1.5$ cm are located at its center with optical properties $\mu_a=\mu_{a0}+\delta\mu_a$ and $\mu_s'=\mu_{s0}'+\delta\mu_s'$. The indices of refraction inside and outside the phantom model were set to $n_{int}=1.33$ and $n_{ext}=1.5$ to simulate the scattering solution and the glass plates of the cuvette used in the real experiments. Assuming a $\delta$-like point source, TPS functions were calculated for the on-axis geometry only.

### A. Comparison of forward simulations based on perturbation theory and FEM model

Forward simulations were based on perturbation theory up to second order for absorption and scattering changes, and up to third order for inhomogeneities representing pure absorbers. Second $[f^{(2)}(t)]$ and third $[f_{aaa}^{(3)}(t)]$ order shape functions were calculated on a personal computer with one Pentium 4 (3 GHz) processor. Dividing each spatial coordinate
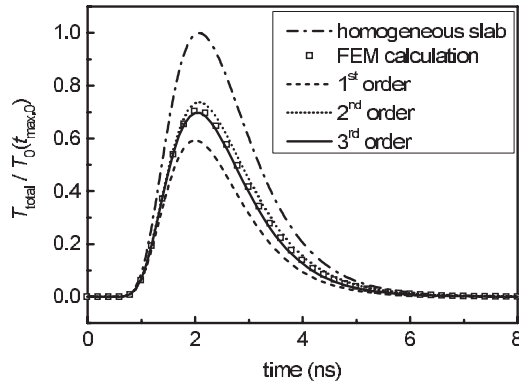
FIG. 1. Simulated time-domain photon flux densities through a partially homogeneous slab bearing a spherical heterogeneity ($R_{imp}$=1.0 cm, $z_{imp}$=3 cm, $d$=6 cm, on-axis geometry, $\mu_{a0}$=0.045 cm$^{-1}$, $\mu'_{s0}$=9.4 cm$^{-1}$, $\delta\mu_a$=+0.07 cm$^{-1}$, $\delta\mu'_s$=0 cm$^{-1}$) using various forward models. All curves are normalized to the amplitude $T_0(t_{\max,0})$ of the photon flux density $T_0$ (dash-dotted line) transmitted through a homogeneous slab, shown for comparison.

$(x,y,z)$ into 11 bins, the kernels of the double (second order) and triple (third order) volume integrals need to be calculated for a total of $11^6$ and $11^9$ voxels, respectively. As expected, not all terms $I^{\alpha_0,\dots,\alpha_N}_{m_0,\dots,m_N}{}^{(N)}$ contribute significantly to the change in the transmitted photon flux density, drastically limiting the number of terms to be evaluated. For example, in third order only 4 terms ($I^{0,0,0,0}_{0,0,0,0}, I^{1,0,0,0}_{0,0,0,0}, I^{0,0,0,1}_{0,0,0,0}, I^{1,0,0,1}_{0,0,0,1}$) contribute significantly to $f^{(3)}_{aaa}(t)$. Taking only two dipoles (photon source and sink), the spherical heterogeneity proper and four mirrored spheres into account, at each time $t$ about 240 s of computational time were required to calculate $f^{(3)}_{aaa}(t)$, whereas second-order shape functions $f^{(2)}(t)$ were evaluated within seconds for a given time $t$, e.g., 9 s for $f^{(2)}_{aa}(t)$ and 22 s for $f^{(2)}_{DD}(t)$. On the other hand, at each time $t$ first-order shape functions $f^{(1)}_a(t)$ and $f^{(1)}_D(t)$ were calculated within 35 ms.

Additionally, FEM simulations were carried out for comparison by numerically solving the diffusion equation, using partial current boundary conditions [34]. The three-dimensional (3D) FEM mesh was generated from tetrahedral elements and was refined in the vicinity of the photon source and within the spheres, in the latter case to account for the size of the spherical inhomogeneities with sufficient precision. A separate mesh was generated for each of the three spheres of different size consisting of about 33 000 nodes and 180 000 elements. The meshes were generated using the software package ANSYS (ANSYS Inc., Canonsburg, PA, USA) and used together with the FEM package TOAST [36,37]. At increments of 10 ps a total of 1150 s of computational time were required to generate an entire profile of transmitted photon flux density extending over 8 ns. For a comparison of transmitted photon flux densities obtained from FEM calculations with analytical results, the FEM photon flux densities had to be shifted in time by several tens of ps to obtain agreement.

To illustrate the convergence of the Born series, Fig. 1 compares time-resolved transmitted photon flux density [e.g.,

$T^{(2)}_{total}(t)=T_0(t)+\delta T^{(1)}_a(t)+\delta T^{(2)}_{aa}(t)$] calculated up to first, second, and third order with FEM simulations representing the true solution of the diffusion equation, assuming a purely absorbing sphere ($\delta\mu_a$=0.07 cm$^{-1}$, $R_{imp}$=1 cm). Computational times (80 time points) amounted to 3 s (first order), 12 min (second order), and 320 min (third order). In addition the photon flux density $T_0(t)$ transmitted through the homogeneous slab is included in Fig. 1 and all results shown are normalized to the maximum of $T_0(t)$, occuring at $t=t_{\max,0}$. As can be seen, first-order perturbation theory underestimates the transmitted photon flux density. The second-order approximation overcompensates this error to some extent, whereas transmitted photon flux density calculated up to third-order almost quantitatively agrees with the FEM result. This behavior illustrates the alternating contributions of odd and even terms to the Born series. An analogous comparison of time-resolved transmitted photon flux densities obtained from first- and second-order perturbation theory with FEM results for a pure scatterer ($R_{imp}$=1 cm) shows almost quantitative agreement ($\delta\mu'_s$=+4 cm$^{-1}$) or a slight overestimation of the amplitude ($\delta\mu'_s$=−4 cm$^{-1}$).

As was mentioned in Sec. II A the innermost volume integrals of the expressions for the second-order shape functions, in particular for the most critical scattering-scattering contribution $f^{(2)}_{DD}(\vec{r}_{det},t)$ are integrable at $\vec{r}_p=\vec{r}_q$ (see Appendix A). In order to check convergence when numerically evaluating the innermost integral for $f^{(2)}_{DD}(\vec{r}_{det},t)$, we assumed typical values for the absorption and reduced scattering coefficients ($\mu_{a0}$=0.045 cm$^{-1}$, $\mu'_{s0}$=9.4 cm$^{-1}$), selected the time $t$=2 ns and a cube of edge length 0.5 cm, centered at $\vec{r}_p=\vec{r}_q$. The value of the innermost integral was evaluated at discretizations ranging between 2 mm and 20 $\mu$m, omitting the central voxel in each case. In this way the discretization error of the innermost integral of $f^{(2)}_{DD}(\vec{r}_{det},t=2$ ns$)$ was found to be 3% and 0.03% at discretizations of 1 mm and 0.1 mm, respectively, illustrating rapid convergence.

Figures 2(a)–2(d) compare transmitted photon flux densities calculated by various orders of perturbation theory including Padé approximants with FEM results over a range of absorption changes $\delta\mu_a$ [Figs. 2(a) and 2(b)] of pure absorbers and changes $\delta\mu'_s$ of the reduced scattering coefficient of pure scatterers [Figs. 2(c) and 2(d)] with radii $R_{imp}$=1 cm [Figs. 2(a) and 2(c)] and $R_{imp}$=1.5 cm [Figs. 2(b) and 2(d)]. In Fig. 2 relative changes $(\Delta T/T_0)(t_{\max,0})=[T_{total}(t_{\max,0})-T_0(t_{\max,0})]/T_0(t_{\max,0})$ of the transmitted photon flux density $T_{total}(t)$ are shown, taken at the time $t=t_{\max,0}$. As can be seen from Figs. 2(a) and 2(b) linear perturbation theory predicts zero transmitted photon flux density for absorption changes $\delta\mu_a$=0.17 cm$^{-1}$ ($R_{imp}$=1 cm) and $\delta\mu_a$=0.06 cm$^{-1}$ ($R_{imp}$=1.5 cm), respectively, and even negative values for absorption changes beyond these values (breakdown limits $L_1$), clearly illustrating the complete breakdown of linear perturbation theory in these cases. Second-order perturbation theory improves the agreement of $\Delta T/T_0$ with the FEM results [Figs. 2(a) and 2(b)], extending the validity of perturbation theory to larger absorption changes. However, for a radius of $R_{imp}$=1 cm ($R_{imp}$=1.5 cm) second-order perturbation theory predicts minima of $\Delta T/T_0$ at absorption changes of $\delta\mu_a^{\min}$=0.10 cm$^{-1}$ ($\delta\mu_a^{\min}$=0.05 cm$^{-1}$). Absorption
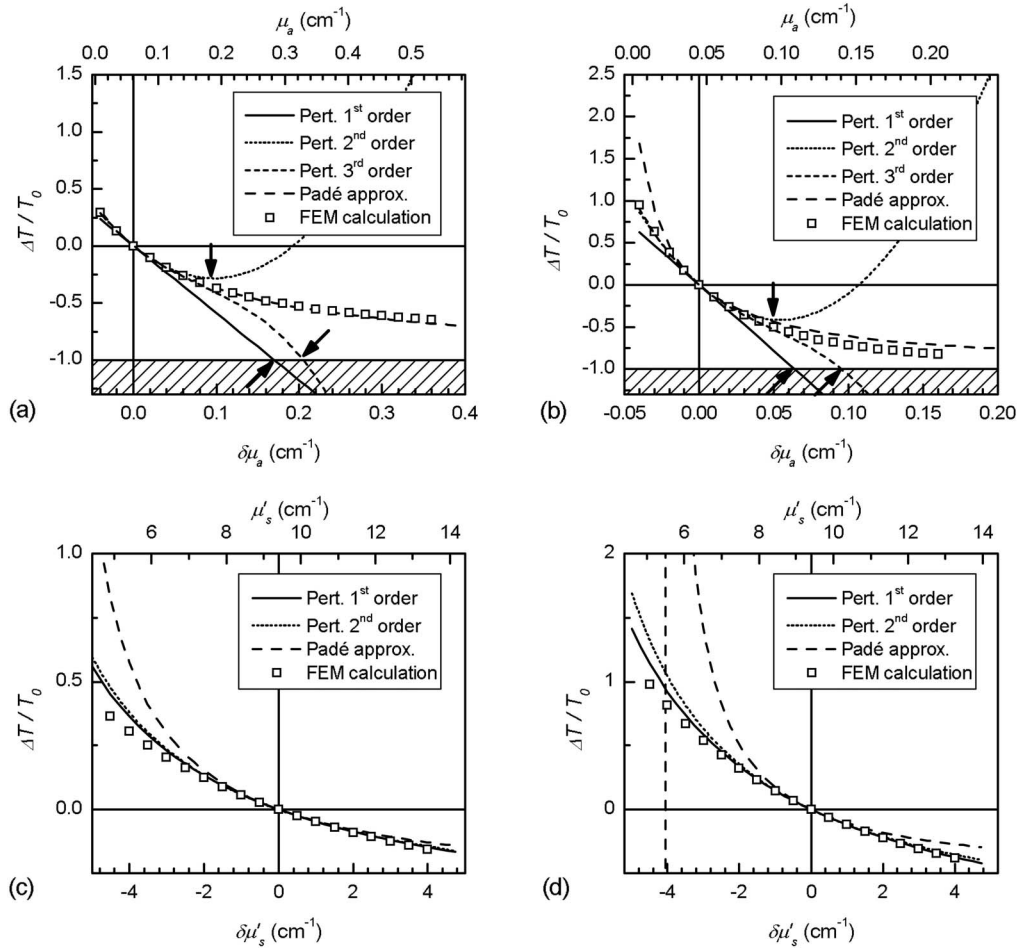
FIG. 2. Normalized changes of transmitted photon flux density $(T_{total} - T_0)/T_0$ through partially homogeneous slab (same geometry and parameters as Fig. 1 unless stated otherwise) at time $t = t_{max,0}$ versus changes in absorption and scattering of spherical heterogeneity over background values. Transmitted flux densities simulated by various forward models assuming (a) radius $R_{imp} = 1.0$ cm, $\delta\mu'_s = 0$ cm$^{-1}$ (pure absorber); (b) radius $R_{imp} = 1.5$ cm, $\delta\mu'_s = 0$ cm$^{-1}$; (c) radius $R_{imp} = 1.0$ cm, $\delta\mu_a = 0$ cm$^{-1}$ (pure scatterer); (d) radius $R_{imp} = 1.5$ cm, $\delta\mu_a = 0$ cm$^{-1}$. Results obtained from third-order perturbation theory are given for pure absorbers only. Breakdown limits of first-, second-, and third-order perturbation theories are indicated by arrows in (a) and (b).

changes of the spherical heterogeneity beyond the breakdown limits $L_2$ will cause transmitted photon flux density to rise again, in contradiction to physical experience, marking the complete breakdown of perturbation theory of second order. It follows from Figs. 2(a) and 2(b) that second-order perturbation theory cannot account for changes $\Delta T/T_0$ < −0.28 ($R_{imp} = 1$ cm) and $\Delta T/T_0$ < −0.42 ($R_{imp} = 1.5$ cm), respectively. Similar to first-order theory, third-order perturbation theory predicts negative values of $\Delta T/T_0$ for absorption changes exceeding $\delta\mu_a = 0.21$ cm$^{-1}$ ($R_{imp} = 1$ cm) or $\delta\mu_a = 0.095$ cm$^{-1}$ ($R_{imp} = 1.5$ cm), again marking the complete breakdown of perturbation theory carried up to third order (breakdown limits $L_3$). It follows from Figs. 2(a) and 2(b) that second and third order extend the validity of first-order theory to some extent. Considering $(\Delta T/T_0)(t)$ at a time $t$ other than $t_{max,0}$, or even the time-integrated transmitted photon flux density $\Delta\bar{T}/\bar{T}_0 = (\bar{T}_{total} - \bar{T}_0)/\bar{T}_0$ for comparison, will cause quantitative changes in Figs. 2(a) and 2(b) but will not affect the general features. When choosing $(\Delta T/T_0)(t)$ at $t > t_{max,0}$ or $\Delta\bar{T}/\bar{T}_0$ for comparison, the breakdown limits $L_1$,

$L_2$, and $L_3$ shift to slightly smaller absorption changes, particularly for the third-order correction, since close to its breakdown limit $\delta\phi^{(3)}_{aaa}(t)$ leads to appreciable changes in the pulse shape of $T_{total}(t)$. In Figs. 2(c) and 2(d) values of $(\Delta T/T_0)(t_{max,0})$ are shown for a range of changes $\delta\mu'_s$ in the reduced scattering coefficient, typically observed in tumors. Within this range, first- and second-order perturbation theory provide reasonably accurate values of $\Delta T/T_0$. From a practical point of view there is little advantage to be expected from a more elaborate perturbation theory covering higher-order corrections of scattering changes.

Besides results of perturbation theory we include in Fig. 2 values of $\Delta T/T_0$ obtained by the method of Padé approximants. This method expresses transmitted photon flux density as

$$T_{Padé} = T_0(1 - \delta T^{(1)}/T_0)^{-1} \qquad (18)$$

and is based on an empirical modification of linear perturbation calculations intended to lift the saturation behavior (see below) of the Born approximation for increased ($\delta\mu_a > 0$)
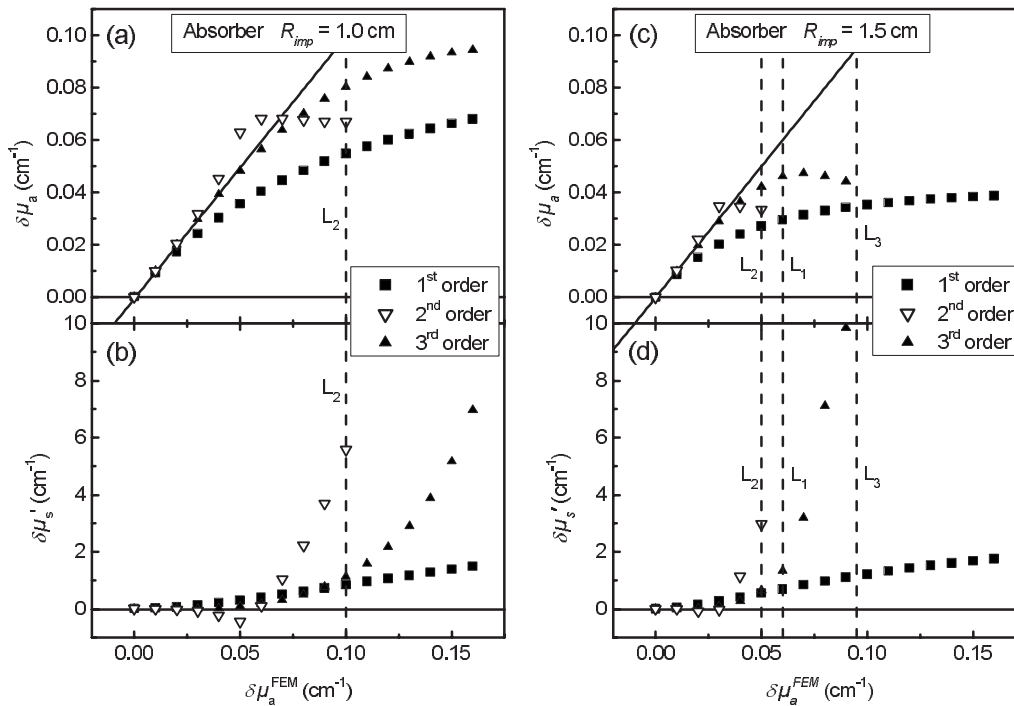
FIG. 3. Reconstruction of optical properties $(\delta\mu_a, \delta\mu_s')$ of spherical heterogeneities derived by fitting results obtained from perturbation theory up to second order in scattering changes $(\delta\mu_s')$ and third order in absorption changes $(\delta\mu_a)$ to simulated FEM data; (a), (c) changes in absorption coefficient $(\delta\mu_a)$ and (b), (d) associated changes in reduced scattering coefficient $(\delta\mu_s')$ obtained from fits versus "true" absorption changes $\delta\mu_a^{FEM}$ used in FEM simulations for pure absorber $(\delta\mu_s'^{FEM}=0)$. Breakdown limits [see Figs. 2(a) and 2(b)] of first-, second-, and third-order perturbation theory are indicated by vertical dashed lines labeled $L_1$, $L_2$, and $L_3$, respectively. Geometry and background optical properties same as for Figs. 1 and 2.

absorption [22]. Computational efforts required for the Padé approximants are the same as for first-order perturbation theory. By definition, Eq. (18) never produces negative values of the transmitted photon flux density in this case. As can be seen from Fig. 2 values of $\Delta T/T_0$ obtained in this way closely approach the FEM results for increased absorption or larger scattering $(\delta\mu_a > 0, \delta\mu_s' > 0)$. However, the expression given in Eq. (18) has a pole for $\delta T^{(1)} > 0$ and, therefore, fails at lower absorption or scattering of the heterogeneity compared to the bulk values. In particular, cysts often exhibiting lower scattering, cannot be analyzed by the Padé approach. On the other hand, tumors that are detected by optical mammography lead to $\delta T^{(1)} < 0$ and the Padé approach is expected to be applicable in these cases.

### B. Inverse problem: Estimating optical properties of inhomogeneities using perturbation theory

We used perturbation theory carried to first and second order in scattering changes $\delta\mu_s'$ and up to third order in absorption changes $\delta\mu_a$ to analyze normalized FEM data $T_{FEM}(t)/T_0(t_{max,0})$ for the optical properties of the spherical inhomogeneities of radii $R_{imp}=1$ cm [Figs. 3(a) and 3(b)] and $R_{imp}=1.5$ cm [Figs. 3(c) and 3(d)]. Only FEM data corresponding to pure absorbers and without any noise added were analyzed in this way. Besides background optical properties, as well as location and size of the spherical inhomogeneities no further prior knowledge was included in the

analysis, i.e., the FEM data were analyzed simultaneously for changes in absorption $(\delta\mu_a)$ and scattering $(\delta\mu_s')$ of the heterogeneities, a common situation encountered when analyzing *in vivo* data. The TPS functions were compared within the range $t_1 \leq t \leq t_2$, where $t_1$ and $t_2$ denote the times on the leading and trailing edge of $T_0(t)$ corresponding to 20% and 5%, respectively, of the maximum amplitude $T_0(t_{max,0})$. Figures 3(a) and 3(c) compare absorption changes $\delta\mu_a$ derived in this way with the values $\delta\mu_a^{FEM}$ used to generate the FEM data, whereas associated reduced scattering coefficients $\delta\mu_s'$ obtained from the fits are illustrated in Figs. 3(b) and 3(d), respectively. Since the FEM data analyzed correspond to pure absorbers these changes in scattering represent artifacts, compensating for model errors to some extent. As can be seen from Fig. 3(a), for the smaller sphere $(R_{imp}=1$ cm) absorption changes $\delta\mu_a$ derived by first-, second-, and third-order perturbation theory quantitatively deviate from the "true" values for $\delta\mu_a^{FEM} \geq 0.03$ cm$^{-1}$, $\delta\mu_a^{FEM} \geq 0.07$ cm$^{-1}$, and $\delta\mu_a^{FEM} \geq 0.08$ cm$^{-1}$, respectively. Likewise, for the larger sphere $(R_{imp}=1.5$ cm) first-, second-, and third-order perturbation theory underestimate changes in absorption for $\delta\mu_a^{FEM} \geq 0.02$ cm$^{-1}$, $\delta\mu_a^{FEM} \geq 0.04$ cm$^{-1}$, and $\delta\mu_a^{FEM} \geq 0.05$ cm$^{-1}$, respectively. The limiting values $\delta\mu_a^{FEM} \approx 0.07$ cm$^{-1}$ (second order, $R_{imp}=1.0$ cm), $\delta\mu_a^{FEM} \approx 0.08$ cm$^{-1}$ (third order, $R_{imp}=1.0$ cm) and $\delta\mu_a^{FEM} \approx 0.04$ cm$^{-1}$ (second order, $R_{imp}=1.5$ cm), $\delta\mu_a^{FEM} \approx 0.05$ cm$^{-1}$ (third order, $R_{imp}=1.5$ cm) are in close agreement with the formal Cauchy convergence criterion

($C_{Cauchy}$=1) deduced above ($\delta\mu_a$=0.071 cm$^{-1}$ for $R_{imp}$ =1 cm, $\delta\mu_a$=0.032 cm$^{-1}$ for $R_{imp}$=1.5 cm). Figures 3(a) and 3(c) illustrate the saturation of the derived changes $\delta\mu_a$ in absorption with increasing true absorption changes $\delta\mu_a^{FEM}$. For example, no values of $\delta\mu_a$ exceeding 0.07 cm$^{-1}$ ($R_{imp}$ =1 cm) and $\delta\mu_a$=0.035 cm$^{-1}$ ($R_{imp}$=1.5 cm) were obtained from the analysis using second-order perturbation theory as forward model. These limits differ somewhat from the limiting values $\delta\mu_a^{min}$ at which the minima occur in Figs. 2(a) and 2(b) which relates to $t_{max,0}$ rather than to the range $t_1 \leq t \leq t_2$. When the absorption change $\delta\mu_a$ reconstructed by second- and third-order perturbation theory levels off [see Figs. 3(a) and 3(c)], a steep rise of the change of the reduced scattering coefficient $\delta\mu_s'$ occurs [Figs. 3(b) and 3(d)]. As pointed out above, nonzero reduced scattering changes are artifacts and transmitted photon flux densities calculated by second- and third-order perturbation theory represent progressively poorer fits to the data beyond the limiting values of $\delta\mu_a^{FEM}$ given above for both radii $R_{imp}$. In Fig. 3 the break-down limits $L_1$, $L_2$, and $L_3$ of first-, second-, and third-order perturbation theory are indicated by vertical dashed lines for comparison.

## IV. PHANTOM MEASUREMENTS AND THEIR ANALYSIS BY VARIOUS FORWARD MODELS

As diffusely scattering phantom we used a rectangular glass cuvette (thickness $d$=6.0 cm) containing dilute milk with spheres of radii 5 mm, 10 mm, and 15 mm, located at its center which were made from agarose gel and served as inhomogeneities [24,38]. The absorption coefficients and reduced scattering coefficients of the various agarose spheres were taken to be the same as those of the corresponding reference slab made from the same batch of material. All reference slabs had virtually the same reduced scattering coefficient $\mu_{s,ref}'$ and their absorption coefficients ranged between $\mu_a^{ref}$=0.08 cm$^{-1}$ and $\mu_a^{ref}$=0.20 cm$^{-1}$. The amounts of water and black India ink added to whole milk (3.5% fat) were chosen to achieve a reduced scattering coefficient of about $\mu_{s0}'$=9.0 cm$^{-1}$ and an absorption coefficient $\mu_{a0}$ =0.043 cm$^{-1}$, typical for breast tissue in the near infrared spectral range.

### A. Phantom measurements and data analysis

All measurements on phantoms were taken at $\lambda$ =785 nm employing a mode-locked Ti:sapphire laser system. TPS functions were measured using a fast photomultiplier and time correlated single photon counting. For recording TPS functions perturbed by the spherical inhomogeneities, the transmitting optical fiber and detecting fiber were positioned opposite to each other on the entrance window and exit window of the cuvette, respectively, arranged such that the center of the spherical heterogeneity was located on the line-of-sight connecting both fibers (on-axis arrangement). TPS functions obtained in this way were analyzed for the optical properties of the heterogeneity by perturbation theory as described in the preceding section. Background optical properties were measured with the aga-

rose spheres removed from the phantom using the model of a homogeneous slab for analysis. Simulated time-resolved photon flux densities were convolved with the measured instrumental response function [typical full width at half maximum (FWHM) 200 ps] prior to fitting simulated data to experimental data.

### B. Optical properties of spherical inhomogeneities from measured and simulated data

Optical properties of the spherical inhomogeneities were derived from measured TPS functions using perturbation theory up to second order in scattering and third order in absorption, as well as employing Padé approximants and the diffraction of DPDW as forward models. The model of diffraction of DPDW expresses time-resolved flux density of photons transmitted through the infinite slab as

$$T_{DPDW}(t) = T_0(t) + T_{inh}(t) \tag{19}$$

where $T_{inh}(t)=T_{inh}(\vec{r}_0,\vec{r}_{imp},\vec{r}_{det},R_{imp},d,\mu_{a0},\mu_{s0}',\mu_a,\mu_s',t)$ represents a correction to the transmitted photon flux density accounting for the presence of the spherical heterogeneity of radius $R_{imp}$ at location $\vec{r}_{imp}$ and can be obtained from a partial wave analysis performed in frequency domain [26,38]. In the infinite medium the model of diffraction of DPDW is exact. To obey the boundary conditions of the infinite slab, the method of mirror sources and sinks is used, and corresponding mirror spheres are generated. Therefore, photon density waves propagating from the mirror sources are diffracted by several spheres sequentially. However, only the first diffraction event is generally taken into account in the analysis and, therefore, only an approximate solution is obtained in this way for the diffraction of DPDW by a spherical heterogeneity in an infinite slab.

Figure 4 compares reconstructed absorption coefficients $\mu_a$ of agarose spheres of various sizes with the absorption coefficient $\mu_a^{ref}$ of the batch material the spheres were made from. Absorption coefficients, represented by solid symbols, were reconstructed from measured time-resolved transmittance using the diffraction of DPDW, the Padé approximants, as well as first-, second-, and third-order perturbation theory as forward models. The measured optical properties of the background medium [$\mu_{a0}$=(0.043±0.002) cm$^{-1}$, $\mu_{s0}'$ =(9.0±0.5) cm$^{-1}$, $D_0$= (0.037±0.002) cm)], as well as the geometry of the phantom, i.e., the size and location of the agarose spheres were included as prior knowledge in the reconstruction. The scattering properties of all agarose reference slabs were determined to be $\mu_{s,ref}'$=(8.9±0.5) cm$^{-1}$ [$D^{ref}$= (0.037±0.002) cm)] and, therefore, the agarose spheres represent pure absorbers to good approximation, yet this information was not included as prior knowledge in the reconstruction, i.e., absorption and reduced scattering coefficients of the agarose spheres were reconstructed simultaneously. As discussed above (cf. Sec. III B) deviations of the reconstructed reduced scattering coefficients of the agarose spheres from the value $\mu_{s,ref}'$=$\mu_{s0}'$ represent artifacts which compensate for model errors. Likewise, absorption coefficients of spherical inhomogeneities of the virtual phantom were reconstructed from FEM data without noise added and
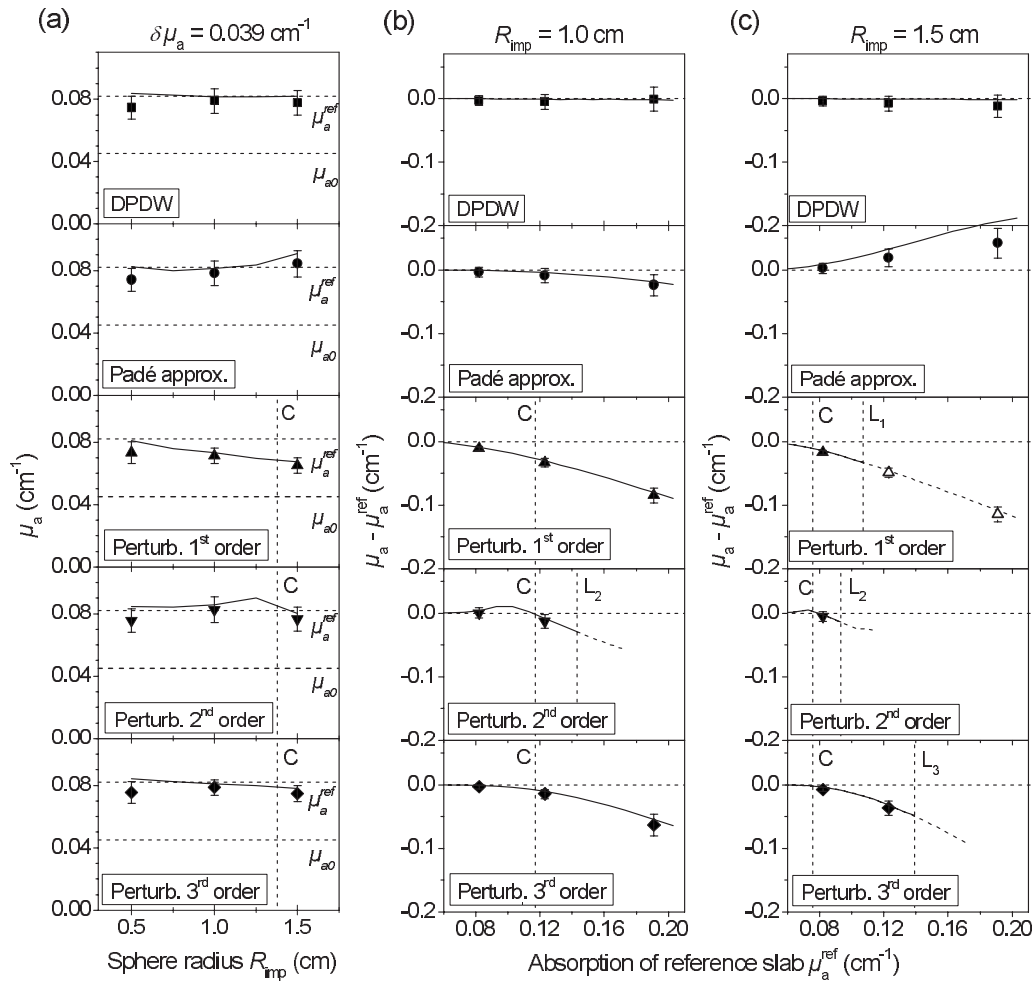
FIG. 4. Reconstructed absorption coefficients $\mu_a$ of pure absorbers of various sizes at center ($z_{imp}=3$ cm) of rectangular physical and virtual phantom ($d=6$ cm, $\mu_{a0}=0.043$ cm$^{-1}$, $\mu'_{s0}=9.0$ cm$^{-1}$, on-axis geometry); absorption coefficients of spherical absorbers reconstructed by fitting results of various forward models to measured temporal point spread functions (symbols) and to simulated (FEM) transmitted photon flux densities (lines); vertical dashed lines labeled $C$ correspond to Cauchy limit $C_{Cauchy}=1$, vertical dashed lines labeled $L_1$, $L_2$, and $L_3$ to breakdown limits of first-, second-, and third-order perturbation theory [see Figs. 2(a) and 2(b)]; (a) reconstructed absorption coefficient of spheres ($R_{imp}=0.5$ cm, 1.0 cm, 1.5 cm) made from same batch of agarose material ($\mu_a^{ref}=0.082$ cm$^{-1}$); absorption coefficients of agarose material and of background medium indicated by horizontal straight lines labeled $\mu_a^{ref}$, $\mu_{a0}$, respectively; (b) difference $\mu_a-\mu_a^{ref}$ between reconstructed absorption coefficient $\mu_a$ and true value of spherical absorbers ($R_{imp}=1.0$ cm); (c) same plot as (b) but for $R_{imp}=1.5$ cm; results of first-, second-, and third-order perturbation theory beyond their breakdown limits indicated as dashed lines (b), (c) and by open symbols (c).

are represented by lines in Fig. 4. To this end transmitted photon flux densities were simulated assuming spherical inhomogeneities with the same scattering properties as the reference slabs (i.e., representing essentially pure absorbers), the same geometry of the phantom, including location of the inhomogeneities and the same optical properties of the background medium as used in the experiments. In Fig. 4 the vertical dashed lines labeled $C$ indicate the Cauchy limit $C_{Cauchy}=\delta\mu_a^{ref}R_{imp}^2/(2D_0)=1$, i.e., beyond which the Cauchy convergence criterion is no longer fulfilled.

In Fig. 4(a) we plot reconstructed absorption coefficients of agarose spheres made from the same batch material [$\mu_a^{ref}=(0.082\pm0.004)$ cm$^{-1}$] and absorption coefficients of spherical pure absorbers with the same absorption properties reconstructed from FEM data versus radius $R_{imp}$. As can be

seen at the smallest radius ($R_{imp}=0.5$ cm) all models used to reconstruct the absorption coefficient from measured data lead to nearly the same value for $\mu_a$ that falls slightly below $\mu_a^{ref}$, represented by the horizontal dashed line. This discrepancy is readily explained taking into account that the radius of the smallest agarose sphere might not be known with sufficient accuracy. For the larger agarose spheres, however, absorption coefficients $\mu_a$ obtained from first-order perturbation theory systematically fall below the reference value $\mu_a^{ref}$. At $R_{imp}=1.5$ cm first-order perturbation theory underestimates $\mu_a$ by about 21%. For these weakly absorbing spheres ($\delta\mu_a=0.039$ cm$^{-1}$) all other forward models yield absorption coefficients in agreement with $\mu_a^{ref}$ within experimental error limits. Absorption coefficients of spherical pure absorbers reconstructed from FEM data provide the same general pic-

ture, supporting our conclusions derived from the analysis of experimental data. In particular, at larger radii first-order perturbation theory fails to correctly deduce the absorption coefficient $\mu_a^{ref}$ of the spherical inhomogeneities from simulated transmitted photon flux densities, systematically underestimating absorption, in agreement with Figs. 3(a) and 3(c). We note in passing that first-, second-, and third-order perturbation theory when used as forward models yield satisfactory fits of calculated transmitted photon flux densities to experimental and simulated data for these weakly absorbing spheres.

In Figs. 4(b) and 4(c) we plot the difference $\mu_a - \mu_a^{ref}$ between reconstructed absorption coefficients and reference values versus $\mu_a^{ref}$ for the two larger spheres separately with radii $R_{imp}=1$ cm [Fig. 4(b)] and $R_{imp}=1.5$ cm [Fig. 4(c)]. Generally, absorption coefficients reconstructed from measured TPS functions and from simulated FEM data convey the same message. In each case the diffraction of DPDW yields the expected absorption coefficient from experimental data within experimental error limits. Likewise, this forward model correctly reconstructs the absorption coefficients of the spherical heterogeneities from simulated (FEM) data. On the other hand, using Padé approximants to reconstruct absorption coefficients from measured or simulated data tends to underestimate absorption of the sphere with $R_{imp}=1$ cm [Fig. 4(b)], but systematically overestimates absorption coefficients of the largest heterogeneity at high absorption [$R_{imp}=1.5$ cm, Fig. 4(c)], consistent with Fig. 2(a) and 2(b), respectively. Again, first-order perturbation theory generally underestimates the absorption coefficient $\mu_a$ of the agarose spheres and, likewise, of spherical inhomogeneities of the virtual phantom. Results of first-order perturbation theory beyond its breakdown limit $L_1$ [see Fig. 4(c)] are indicated by open symbols (experimental data) and by dashed lines (simulated data). Second-order perturbation theory yields agreement within experimental accuracy at the lowest absorption ($\mu_a^{ref}=0.082$ cm$^{-1}$) for all agarose spheres investigated ($R_{imp}=0.5$ cm, 1.0 cm, 1.5 cm) and at the next higher absorption coefficient $\mu_a^{ref}=0.124$ cm$^{-1}$ for the agarose spheres with radius $R_{imp}=0.5$ cm (not shown) and $R_{imp}=1$ cm. For all other experimental and simulated situations related to Figs. 4(b) and 4(c) the absorption coefficient $\mu_a^{ref}$ exceeds the breakdown limits $L_2$ of second-order perturbation theory, i.e., at which the minima [see Figs. 2(a) and 2(b)] in $\Delta T/T_0=(T_{total}^{(2)}-T_0)/T_0$ occur. These limits are indicated in Figs. 4(b) and 4(c) by vertical dashed lines. Beyond these limits no satisfactory fits of time-resolved photon flux densities calculated by second-order perturbation theory to simulated data could be obtained and absorption coefficients included in Figs. 4(b) and 4(c) beyond these limits are indicated by dashed lines. For example, at $\mu_a^{ref}=0.124$ cm$^{-1}$ a sphere of radius $R_{imp}=1.5$ cm causes a reduction of the peak value of the transmitted time-resolved photon flux density from the homogeneous value beyond the limit $\Delta T/T_0=-0.42$ that can at most be explained by second-order perturbation theory [see minimum in Fig. 2(b)]. For $R_{imp}=1$ cm third-order perturbation theory yields acceptable fits of calculated time-dependent photon flux densities to measured TPS functions or simulated FEM data over the full

range of absorption coefficients $\mu_a^{ref}$ covered in Fig. 4(b), consistent with Figs. 2(a) and 3(b). However, higher absorption coefficients $\mu_a$ are considerably underestimated, e.g., at $\mu_a^{ref}=0.19$ cm$^{-1}$ by about 30%. This picture progressively deteriorates for the largest sphere ($R_{imp}=1.5$ cm). As discussed above, third-order perturbation theory totally breaks down at $\mu_a^{ref}=0.14$ cm$^{-1}$ (breakdown limit $L_3$). However, when approaching this limit ($\mu_a^{ref}<0.14$ cm$^{-1}$) third-order contributions considerably modify the shape of the transmitted photon flux density, and calculated photon flux densities no longer show the typical pulse shape of TPS functions, leading to unacceptable fits to measured data or FEM data. It follows that model errors can no longer be compensated for by a change in the reduced scattering coefficient from the true value to produce the correct line shape. Consistent with Fig. 3(d), results of third-order perturbation theory beyond the breakdown limit $L_3$ are indicated by dashed lines in Fig. 4(c). Furthermore, for the largest agarose sphere ($R_{imp}=1.5$ cm) with the highest absorption coefficient ($\mu_a^{ref}=0.19$ cm$^{-1}$) studied experimentally the ratio $C_{Cauchy}=\delta\mu_a^{ref}R_{imp}^2/(2D_0)$ associated with the Cauchy convergence criterion amounts to about 5, indicating severe convergence problems. Although second- and third-order extend the range of validity of perturbation theory to cover larger absorption changes and sizes of the (spherical) inhomogeneities relevant for optical mammography, it follows from Figs. 4(b) and 4(c) that the gain in accuracy of the numerical results over those obtained from simple first-order theory is limited, a conclusion also evident from Figs. 2(a) and 2(b). In summary, the reconstruction of optical properties of spherical inhomogeneities from experimental data yields the same ranges of validity of first-, second-, and third-order perturbation theory as obtained from simulated FEM data. Taking experimental uncertainties of phantom data into account, amounting typically to 10–15 %, the limit of validity of higher-order perturbation analyses may extend in practice to slightly higher values of $\delta\mu_a$.

We conclude this section by commenting on Fig. 4 of Ref. [24] which is closely related to our Fig. 4. Without critically assessing the results of his analysis of measured TPS functions, Wassermann included reconstructed absorption coefficients of spherical heterogeneities using second-order [see Fig. 4(b), $\mu_a^{ref}=0.19$ cm$^{-1}$ and Fig. 4(c), $\mu_a^{ref}=0.124$ cm$^{-1}$, 0.19 cm$^{-1}$ of Ref. [24]] and third-order [see Fig. 4(c), $\mu_a^{ref}=0.19$ cm$^{-1}$ of Ref. [24]] perturbation theory that were beyond their ranges of validity as discussed above and were therefore omitted in our Figs. 4(b) and 4(c). Furthermore, whereas our results clearly show the superiority of DPDW as forward model to reconstruct the absorption coefficient of spherical absorbers from phantom measurements, in Fig. 4 of Ref. [24] absorption coefficients reconstructed by using DPDW differ appreciably from the true absorption coefficients and are thus in error.

## V. TUMOR OPTICAL PROPERTIES FROM PERTURBATION THEORY, PADÉ APPROXIMANTS, AND DIFFRACTION OF DPDW

Limitations of perturbation theory to derive tumor optical properties from optical mammograms will depend on tumor
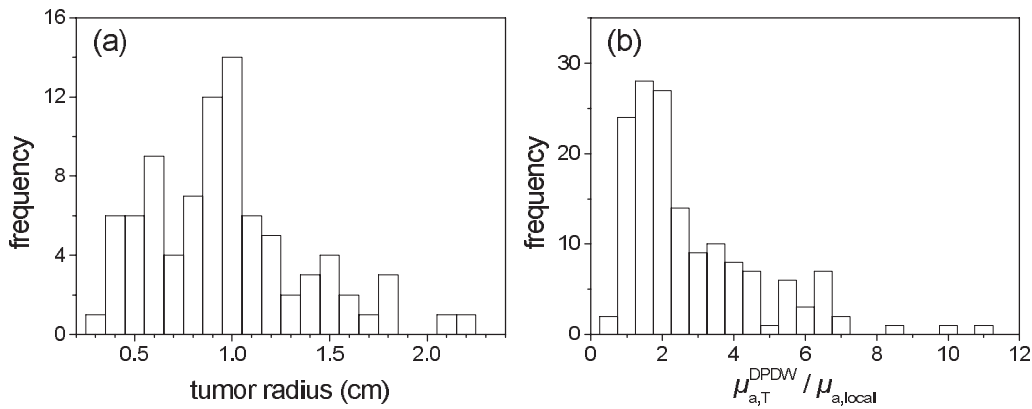
FIG. 5. Histograms (number of cases) of (a) histologically determined tumor size (isovolumetric radius) of 87 breast carcinomas and (b) of tumor absorption contrast $\mu_{a,T}^{DPDW}/\mu_{a,local}$ at 785 nm obtained from analysis of 151 optical projection mammograms.

and background optical properties, in particular on tumor contrast and background inhomogeneity as well as on tumor size and tumor location. Although phantom measurements yield insights into the limitations of the various methods of analysis, such measurements cannot mimic entirely the *in vivo* situation. In order to assess to what extent perturbation theory carried up to various orders is suited to derive tumor optical properties, analysis of a large number of optical mammograms has been performed. For this purpose we use perturbation theory as well as Padé approximants to reanalyze *in vivo* data from our previous clinical trial on optical mammography [6] to derive tumor optical properties at 785 nm and compare the results with the tumor absorption coefficients $\mu_{a,T}^{DPDW}$ obtained previously [29].

During the clinical trial craniocaudal (cc) and mediolateral (ml) projection optical mammograms of 154 patients, suspected to have breast cancer were recorded at selected near infrared wavelengths (e.g., 670 nm, 785 nm) [6]. Among the 96 tumors validated by histology that had been investigated at two or three wavelengths, 88 tumors could be detected retrospectively in projection optical mammograms (70 tumors in cc and ml projections, additional 18 tumors in one projection only). Apart from one case, absorption ($\mu_{a,T}^{DPDW}$) and reduced scattering ($\mu_{s,T}^{\prime DPDW}$) coefficients of these tumors were derived from temporal point spread functions recorded at the tumor site and amounting to typically 250 000 photons detected at each wavelength. A total of 151 projection mammograms of tumor-bearing breasts were analyzed successfully in this way for tumor optical properties [29]. To this end the compressed breast was modeled as partially homogeneous infinite slab of thickness $d$ with background optical properties $\mu_{a,local}$, $\mu_{s,local}^{\prime}$ employing the diffraction of DPDW by a spherical heterogeneity as forward model representing the tumor. The tissue optical properties $\mu_{a,local}$, $\mu_{s,local}^{\prime}$ were derived from temporal point spread functions measured within an area of the particular optical mammogram which surrounded the tumor, and the actual breast thickness at the tumor site was inferred from first moments of measured TPS functions as described in Ref. [13]. Effective tumor radii $R_T$, taken from pathology, and tumor locations $z_T$ along the compression direction, deduced from off-axis optical scans of the tumor region, were included in

the analysis as prior knowledge, whenever available [29]. For illustration, Figs. 5(a) and 5(b) display histograms of effective tumor radii $R_T$, and tumor absorption contrast, respectively, of the 151 tumor-bearing mammograms. Tumor absorption contrast, expressed as $\mu_{a,T}^{DPDW}/\mu_{a,local}$ (785 nm), was reported to be about 2 on average at 785 nm [29,39]. The effective tumor radius of an isovolumetric sphere was calculated from tumor extensions provided by histopathology. For the tumors considered here the median of the ratio of long to short extensions amounted to about 1.3.

To analyze the *in vivo* data by perturbation theory, first-order $[f^{(1)}(t)]$, second-order $[f^{(2)}(t)]$, and third-order $[f_{aaa}^{(3)}(t)]$ shape functions [Eqs. (6)–(11)] were calculated for 148 tumor bearing projection mammograms that had previously been analyzed by the diffraction model at tolerable $\chi^2$ values ($\chi^2 \leqslant 100$). For our present analysis the same tissue model was adopted as before, i.e., in each case we modeled the compressed tumor-bearing breast as partially homogeneous infinite slab with a spherical heterogeneity representing the tumor, used the same breast thickness $d$ at the tumor site, the same (local) background optical properties $\mu_{a,local}$, $\mu_{s,local}^{\prime}$, the same effective tumor radius $R_T$, and the same tumor location $z_T$ along the compression direction. First-, second-, and third-order shape functions were calculated for each mammogram, requiring typically between 3 and 8 hours per mammogram to compute the entire shape function $f_{aaa}^{(3)}(t)$. Shape functions were subsequently used in fits of transmitted photon flux density $T_{total}^{(pert)}(t)$, e.g.,

$$T_{total}^{(2)}(t) = T_0(t) + \delta\mu_{a,T}^{(2)}f_a^{(1)}(t) + \delta D_T^{(2)}f_D^{(1)}(t) + (\delta\mu_{a,T}^{(2)})^2 f_{aa}^{(2)}(t)$$
$$+ \delta\mu_{a,T}^{(2)}\delta D_T^{(2)}\{f_{aD}^{(2)}(t) + f_{Da}^{(2)}(t)\} + (\delta D_T^{(2)})^2 f_{DD}^{(2)}(t),$$

convolved with the instrumental response function to derive tumor optical properties $\mu_{a,T}^{(pert)} = \mu_{a,local} + \delta\mu_{a,T}$ and $\mu_{s,T}^{\prime(pert)}$ $[\mu_{s,T}^{\prime(pert)} = 1/(3D_T^{(pert)})]$ from the same measured data as analyzed previously, i.e., from temporal point spread functions recorded at the tumor site with source and detector optical fibers opposing each other (on-axis geometry). Third-order transmitted photon flux density $T_{total}^{(3)}(t)$ was calculated up to third order in absorption changes but only to second order in scattering changes. This approach is justified since scattering
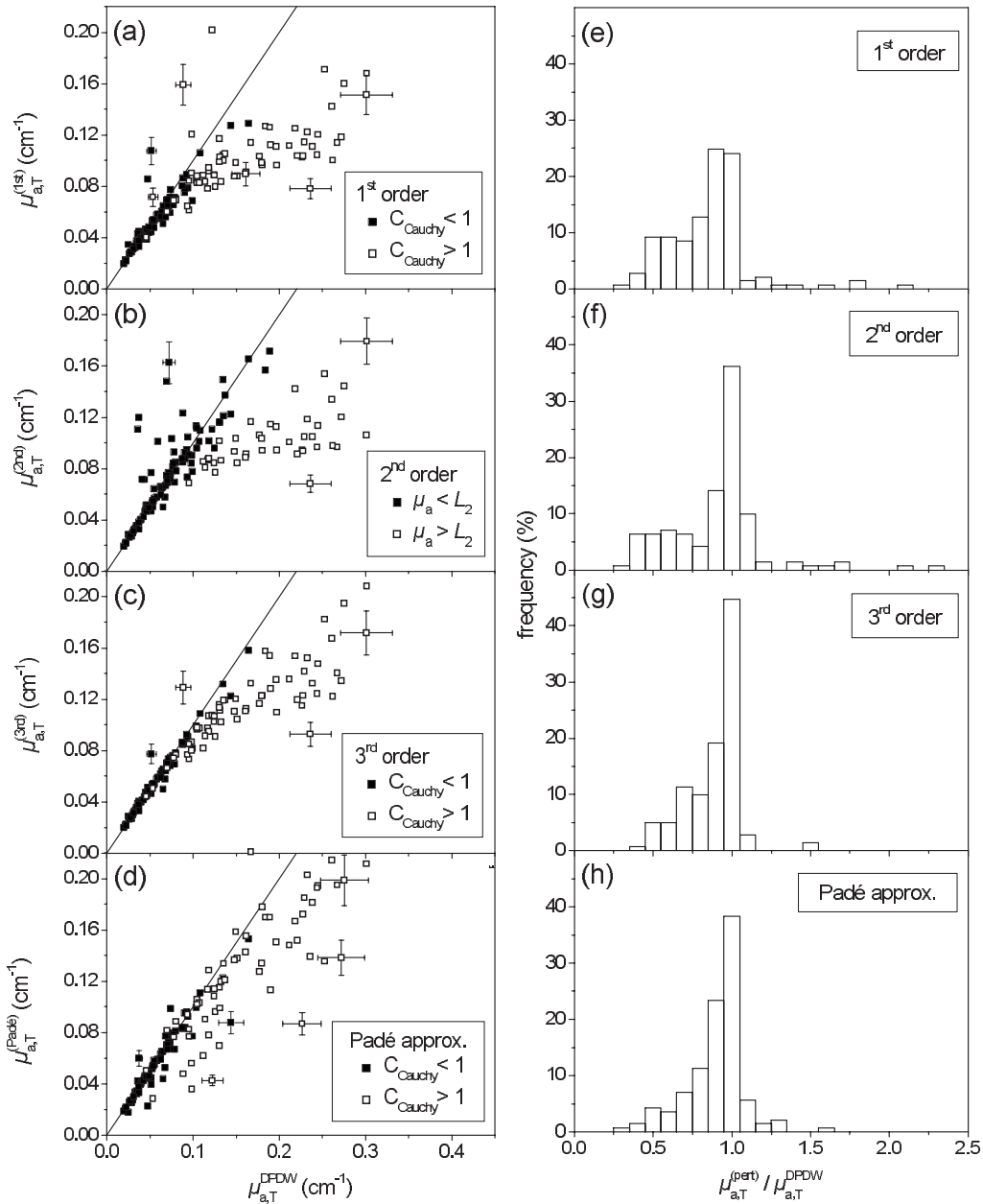
FIG. 6. Scatter plots of tumor absorption coefficients from perturbation theory versus corresponding reference values obtained by the diffraction model (left column) and related histograms displaying (normalized) frequency of tumor absorption coefficients normalized to reference values (right column); (a), (e) first-order, (b), (f) second-order, (c), (g) third-order perturbation theory, (d), (h) Padé approximants. Data refer to 141 optical mammograms, open symbols to absorption coefficients (reference values) above Cauchy limit $C_{Cauchy}=1$ (first-, third-order perturbation theory, Padé approximants) or above limit $L_2$ (second-order perturbation theory). Error bars indicated in (a)–(d) for arbitrarily selected data points correspond to an estimated statistical uncertainty of 10%.

coefficients of breast carcinomas are known to differ from those of surrounding healthy tissue by some 10% only [29]. Tumor optical properties derived from measured data by perturbation theory or the diffraction model might be in error because of the crude tissue model used and because of missing or inaccurate prior knowledge on tumor size ($R_T$), tumor shape, and tumor location ($z_T$). However, within the tissue model adopted, diffraction theory is accurate to good approximation and hence our previous results ($\mu_{a,T}^{DPDW}$, $\mu_{s,T}'^{DPDW}$) on tumor optical properties were taken as reference.

The left-hand side of Fig. 6 compares absorption coefficients $\mu_{a,T}^{(pert)}$ and $\mu_{a,T}^{(Padé)}$ with the diffraction results $\mu_{a,T}^{DPDW}$ at 785 nm, the histograms on the right-hand side illustrate (relative) frequencies at which absorption coefficients normalized to the diffraction results occur that were obtained by perturbation theory ($\mu_{a,T}^{(pert)}/\mu_{a,T}^{DPDW}$) or by Padé approximants ($\mu_{a,T}^{(Padé)}/\mu_{a,T}^{DPDW}$). Among the 148 projection mammograms analyzed by the diffraction model ($\chi^2 \leq 100$), only 141 mammograms could be analyzed by first-order and third-order perturbation theory at tolerable $\chi^2$ values ($\chi^2 \leq 100$) and,

therefore, Fig. 6 includes the results on only 141 tumor-bearing mammograms. On the other hand, second-order analyses of these mammograms yielded values of $\chi^2 \leq 100$ in 122 cases only. For the Padé approximants 137 out of the 141 mammograms could be analyzed at tolerable $\chi^2$ values, whereas in the four remaining cases $\chi^2$ exceeded the value of 100.

In general, simulated transmitted photon flux densities obtained from first- and third-order perturbation theory are better suited to account for measured temporal point spread functions within experimental uncertainties than those calculated from second-order theory. More precisely, diffraction theory yielded fits with $\chi^2$ values $\chi^2 \leq 10$ in about 87% of the 141 cases, first- and third-order perturbation theory achieved satisfactory fits ($\chi^2 \leq 10$) in 84% of the mammograms studied, whereas this was true in only 50% of the cases analyzed by second-order perturbation theory. In the remaining cases the fairly large $\chi^2$ values encountered indicate that the Born series did not allow to fully reproduce measured temporal point spread functions within experimental errors. This is particularly true for second-order perturbation theory which cannot account for the reduced transmittance caused by strongly absorbing lesions of sufficient size as shown in Sec. III A when discussing the minima of the second order results illustrated in Figs. 2(a) and 2(b). As can be seen from Figs. 6(a)–6(c) at rather low tumor absorption ($\mu_{a,T}^{DPDW} \leq 0.08$ cm$^{-1}$) results of perturbation theory $\mu_{a,T}^{(pert)}$ generally agree with absorption coefficients $\mu_{a,T}^{DPDW}$, and in these cases third-order perturbation theory generally improves the agreement with $\mu_{a,T}^{DPDW}$ over first-order results. At higher absorption ($\mu_{a,T}^{DPDW} \gtrsim 0.08$ cm$^{-1}$) first- and second-order coefficients $\mu_{a,T}^{(pert)}$ saturate. Hence, first- and second-order perturbation theory generally underestimate tumor absorption considerably at higher absorption coefficients $\mu_{a,T}^{DPDW}$. Saturation is less pronounced for third-order absorption coefficients [Fig. 6(c)] and the onset of saturation appears to occur at somewhat higher absorption values ($\mu_{a,T}^{DPDW} > 0.10$ cm$^{-1}$). To some extent, Figs. 6(a)–6(c) mimic the results of perturbation theory illustrated in Figs. 3(a) and 3(c).

The large data scatter of the first-and second-order perturbation results observed for $\mu_{a,T}^{DPDW} \gtrsim 0.10$ cm$^{-1}$ and of the third-order absorption coefficients encountered for $\mu_{a,T}^{DPDW} \gtrsim 0.15$ cm$^{-1}$ indicates that perturbation theory is no longer suited to robustly analyze measured temporal point spread functions for tumor optical properties at higher absorption values. In order to illustrate this point we calculated the expression $C_{Cauchy} = |\mu_{a,T}^{DPDW} - \mu_{a,local}| R_T^2 / (2D_0)$ [cf. Eq. (17)] for each case included in Fig. 6 to check whether the Cauchy convergence criterion for the Born series of a pure absorber was met [$C_{Cauchy} < 1$, filled symbols, Figs. 6(a), 6(c), and 6(d) or not [$C_{Cauchy} \geq 1$, open symbols, Figs. 6(a), 6(c), and 6(d)]. It should be noted, however, that tumors generally differ both in absorption as well as scattering from the surrounding tissue and, therefore, the convergence criterion given in Eq. (17) might not be strictly applicable. As can be seen from Figs. 6(a) and 6(c), apart from a few exceptions first- and third-order absorption coefficients that deviate considerably from the diffraction results are associated with a value of the Cauchy criterion larger than 1, indicating prob-

lems with the convergence of the Born series in these cases. Likewise, for each of the 141 mammograms we investigated whether second-order perturbation theory was applicable or broke down entirely, i.e., whether $\delta\mu_{a,T}^{DPDW} = \mu_{a,T}^{DPDW} - \mu_{a,local}$ is below or above $\delta\mu_a^{min}$ at which the minimum of $\Delta T^{(2)}/T_0$ occurs [breakdown limit $L_2$, cf. Figs. 2(a) and 2(b)]. To this end the relative change in transmittance $\Delta T^{(2)}/T_0 = [T_{total}^{(2)}(t_{max,0}) - T_0(t_{max,0})]/T_0(t_{max,0})$ was calculated at the tumor site as a function of $\delta\mu_a = \mu_{a,T} - \mu_{a,local}$ and evaluated at the time $t_{max,0}$ corresponding to the maximum of the background transmittance $T_0(t)$ using second-order perturbation theory, again assuming tumors to be pure absorbers. Open symbols in Fig. 6(b) correspond to mammograms for which $\delta\mu_{a,T}^{DPDW} \geq \delta\mu_a^{min}$, closed symbols to mammograms with $\delta\mu_{a,T}^{DPDW} < \delta\mu_a^{min}$. It follows from Fig. 6(b) that most of the second-order results that deviate significantly from the diffraction results are associated with cases for which second-order perturbation theory is no longer applicable because of strong tumor absorption and/or large tumor size. Some of the exceptions appearing in Fig. 6(b) (filled symbols deviating considerably from straight line) might be explained by the different assumptions underlying the analysis for tumor optical properties and the criterion for the breakdown of second-order perturbation theory derived in Sec. III A. As was noted above, tumors generally differ both in absorption and scattering from the surrounding tissue and tumor optical properties are derived from the entire temporal profile of the transmitted laser pulse, whereas the criterion for breakdown of second-order perturbation theory applies to pure absorbers and is based on the change in the amplitude of the transmitted pulse.

As can be seen from Fig. 6(d), absorption coefficients $\mu_{a,T}^{(Padé)}$ agree with the diffraction results at lower tumor absorption only and generally underestimate tumor absorption at higher absorption levels. On average, Padé absorption coefficients marked by open symbols are lower than the diffraction results by 17%. Most of the data shown in Fig. 6(d) that fall below $\mu_{a,T}^{DPDW}$ correspond to tumors with radii $R_T \leq 1.2$ cm. This situation should be compared with the one encountered in Fig. 4(b) where the method of Padé approximants is seen to underestimate absorption coefficients of the medium-sized ($R_{imp} = 1$ cm) heterogeneity at higher absorption values.

The histograms of $\mu_{a,T}^{(pert)}/\mu_{a,T}^{DPDW}$ and $\mu_{a,T}^{(Padé)}/\mu_{a,T}^{DPDW}$ shown on the right-hand side of Fig. 6 quantify some of the conclusions discussed above. All histograms are skewed towards ratios smaller than 1 illustrating the saturation of the perturbation results observed for increasing tumor absorption. Besides one or two large bins at the center, the frequencies at which $\mu_{a,T}^{(pert)}/\mu_{a,T}^{DPDW}$ and $\mu_{a,T}^{(Padé)}/\mu_{a,T}^{DPDW}$ occur are broadly distributed. The center bin corresponds to mammograms for which the perturbation and Padé results agree with the tumor absorption coefficients within ±5% obtained by the diffraction model. The center bin is seen to rise for higher orders of perturbation theory and comprises about 24% [first order, Fig. 6(e)], 36% [second order, Fig. (6)], 45% [third order, Fig. 6(g)], and 38% [Padé, Fig. 6(h)] of all (141) cases. Many of the mammograms with tumor absorption coefficients $\mu_{a,T}^{DPDW} \leq 0.08$ cm$^{-1}$ contribute to the center bin as

TABLE II. Fractions of optical mammograms (141) analyzed by various forward models for tumor optical properties agreeing with reference values within 10% or 25%.

| Forward model | Percentage of optical mammograms | |
|---|---|---|
| Perturbation theory | Deviation ±10% | Deviation ±25% |
| First order | 35% | 65% |
| Second order | 50% | 66% |
| Third order | 57% | 77% |
| Padé approx. | 55% | 80% |

can be seen from the left-hand side of Fig. 6. The rise of the center bin illustrates the improvement in the accuracy of the tumor absorption coefficients that is achieved when higher-order perturbation theory is still applicable, consistent with our discussion of Figs. 6(a)–6(c). Table II lists the percentages of optical mammograms that were analyzed for tumor optical properties by perturbation theory and Padé approximants within the adopted tissue model and with the prior knowledge included, yielding absorption coefficients within ±10% and ±25% of the diffraction results taken as reference. Even accepting deviations of ±25% from the value $\mu_{a,T}^{DPDW}$ that correspond to its estimated overall uncertainty (see below), first-order perturbation theory fails to accurately account for tumor absorption in about 35% of all cases and this fraction decreases only moderately for second-order (34%) and third-order (23%) perturbation theory. Although first-order Born approximation or Rytov approximation are widely used as forward models to reconstruct tissue (tumor) optical properties from time-domain or frequency-domain data, our results on the accuracy of tumor absorption coefficients derived by first-order perturbation theory question the validity of these forward models to analyze optical mammograms for lesion optical properties. The histogram obtained for Padé approximants is very similar to that for third-order absorption coefficients, i.e., within the range of validity of third-order perturbation theory the Padé approximants may be used to determine tumor optical properties with much lower computational efforts, however, leading to erroneous results when lesion absorption and scattering is below that of the surrounding tissue.

Although the diffraction model itself is accurate to good approximation the underlying tissue model inadequately accounts for the complexity of a tumor-bearing compressed breast, as was mentioned above. Furthermore, inaccurate prior knowledge included in the analysis, e.g., on tumor size, will translate into uncertainties of the optical properties $\mu_{a,T}^{DPDW}$, $\mu'^{DPDW}_{s,T}$ derived, affecting the comparison with the perturbation results to some extent. The effect of uncertainties in tumor radii and tumor position along the compression direction on tumor optical properties $\mu_{a,T}^{DPDW}$, $\mu'^{DPDW}_{s,T}$ was studied in Ref. [29]. In general, tumor radii obtained from histopathology after surgery or from x-ray, magnetic resonance (MR), and ultrasound (US) mammograms were found to correlate with tumor radii estimated from optical mammograms [10]. However, because of the different contrast mechanisms underlying x-ray, MR, US, and optical mammo-

grams, tumor radii derived by the various imaging techniques may differ in selected cases. To estimate the effect of uncertainties in tumor radii on the comparison of tumor optical properties derived by the diffraction and perturbation models, we have changed tumor radii by up to 20% and generated figures such as Fig. 6(a); although the comparison between first-order and diffraction tumor absorption coefficients is affected quantitatively by changes in the tumor radii assumed, the same qualitative results were obtained as the ones illustrated in Fig. 6(a). Reducing tumor radius results in larger tumor absorption coefficients $\mu_{a,T}^{DPDW}$ and hence saturation of first-order results is more pronounced as in Fig. 6(a). The opposite holds true when inreasing tumor size and the same general behavior is to be expected for higher-order perturbation results. Therefore, our main conclusions are unaffected by uncertainties of the prior knowledge included to a large extent since the same prior knowledge was used for the various methods of analysis. Previously the overall uncertainty of diffraction tumor optical properties due to uncertainties in tumor volume, tumor shape, and tumor location $z_T$ was estimated to be about 25% on average [29]. It follows that the right-hand column of Table II corresponds to the fraction of optical mammograms the perturbation results of which differ from the diffraction results by (relative) amounts corresponding to the uncertainties of tumor optical properties derived by the diffraction model taken as reference.

Figure 6 compares absolute values of tumor absorption coefficients obtained by perturbation theory and by the diffraction model. When normalizing tumor absorption coefficients to local background values $(\mu_{a,T}^{(pert)}/\mu_{a,local}, \mu_{a,T}^{DPDW}/\mu_{a,local})$ we observe first, second, and third order results to start to saturate at about $\mu_{a,T}^{(pert)}/\mu_{a,local}$ =1.5, 2, and 2.5, respectively. Furthermore, in this section we discussed only mammograms taken at 785 nm, however, the same conclusions were drawn when analyzing *in vivo* data at 670 nm.

## VI. SUMMARY AND CONCLUSION

We evaluated second- and third-order time-domain perturbation theory on virtual and real breastlike phantoms as well as on *in vivo* data and quantitatively explored to what extent higher- (second, third) order perturbation theory is suited to derive optical properties of breast tumors.

By reconstructing the absorption coefficient $\mu_a$ of spherical heterogeneities of various sizes from simulated or measured time-domain phantom data using first-, second-, and third-order perturbation theory as forward models, first order was shown [see Sec. III B, Fig. 3(a)] to be valid up to $\delta\mu_a$ $\approx 0.03$ cm$^{-1}$ ($R_{imp}$=1 cm), but deviating at even smaller absorption changes for larger radii. Beyond this value ($\delta\mu_a$ >0.03 cm$^{-1}$) first-order perturbation theory considerably underestimates absorption changes. On the other hand, second- and third-order perturbation theory starts to break down, i.e., saturates, at $\delta\mu_a \approx 0.07$ cm$^{-1}$ (second order) and $\delta\mu_a$ $\approx 0.08$ cm$^{-1}$ (third order) for $R_{imp}$=1 cm, again at even lower ratios for larger radii. On average, at 785 nm the change of the absorption coefficient amounts to about $\delta\mu_a$

$\approx 0.06$ cm$^{-1}$ for breast tumors [29]. From this value together with the broad biological variability of tumor sizes and optical properties our phantom results suggest even third-order perturbation theory to underestimate tumor absorption coefficients for a considerable fraction of cases.

To further quantify to what extent perturbation theory allows one to accurately determine optical properties of tumors that are generally detected by (scanning) optical mammography we reanalyzed 141 optical mammograms of 87 patients carrying a tumor that had been validated by histology [29]. Using tumor optical properties obtained from the diffraction model of DPDW as reference and allowing absorption coefficients obtained from perturbation theory or Padé approximants to deviate from the reference by as much as ±25%, first-, second-, and third-order perturbation theory was found to yield accurate tumor absorption coefficients in about 65%, 66%, and 77% of all cases, respectively, with the fraction of 80% observed for the Padé approximants being close to that of third-order theory. In the remaining cases perturbation theory considerably underestimates tumor absorption. The considered deviation of ±25% corresponds to the estimated overall uncertainty of the reference value. Saturation of the (normalized) tumor absorption coefficient $\mu_{a,T}^{(pert)}/\mu_{a,local}$ derived from perturbation theory was observed to set in at ratios $\mu_{a,T}^{DPDW}/\mu_{a,local}$ of about 1.5 (first order), 2 (second order), and 2.5 (third order). Notably, absorption coefficients of tumors were reported to be larger than the background absorption by a factor of about 2 on average, however, exhibiting large data scatter [29,39]. Among the 65% of cases with rather accurate first-order results the third order theory improves the accuracy of tumor absorption and reduced scattering coefficients with respect to the reference data.

In general, there are various theoretical approaches available based on time-domain diffusion theory to simulate light propagation through (thick) biological tissue and to estimate optical properties of tumors. Numerical integration of the time-dependent diffusion equation by FEM methods which was used as reference method in Sec. III allows to accurately calculate the time-dependent photon flux density transmitted through a (finite) slab for arbitrary distributions of the absorption and reduced scattering coefficients. However, FEM calculations are presently too time consuming to fit this forward model to measured TPS functions to deduce absorption and reduced scattering coefficients of heterogeneities, e.g., of tumors. On the other hand, moments of transmitted photon flux densities calculated by FEM and of measured TPS functions could be compared to deduce optical properties rather than the entire pulse profile. Analytical solutions of the diffusion equation lend themselves as forward model to be used in fit procedures. Solutions of the diffusion equation representing the diffraction of DPDW are restricted to a single spherical heterogeneity. In contrast, perturbation theory can account for several embedded inhomogeneities of arbitrary shapes, yet within a limited range of absorption changes and sizes. The empirical nonlinear Padé approach allows to deduce optical properties of strongly absorbing lesions beyond the validity of second-order perturbation theory, yet fails to correctly account for lesions with lower absorption or lower scattering, such as cysts. While first-order perturbation theory is generally not suited to quantitatively deduce tumor optical properties from optical mammograms, and second-order perturbation theory does not allow to correctly fit the transmitted pulse shape in many cases, perturbation theory carried up to second order in scattering and to third order in absorption yields acceptable results in as much as 77% of all cases investigated. Although data scatter was observed to be larger when using Padé approximants as forward model compared to third-order perturbation theory its significantly lower computational load makes the Padé approximants to be the preferred choice when analyzing optical properties of nonspherical lesions as long as cases with lower absorption and large scattering changes can be avoided. However, when the true shape of the tumor in the slightly compressed breast is not precisely known and a spherical tumor shape is assumed for simplicity the diffraction of photon density waves is the forward model of choice, being accurate and computationally not demanding.

## APPENDIX A

Below we list analytical expressions for the first- and second-order contributions $I(\vec{r}_{det},t)$ to the transmitted photon density. In Table I the distances, vectors, and their dot products are defined which are consistent with the notation of Ref. [24]. In addition, the following abbreviations are used:

$$g_1(a,b) = 1 + \frac{(a-b)^2}{ab}, \quad g_2(a,b) = \frac{(a+b)}{a^2b^2},$$

$$g_3(a,b) = 2b^2 + (a-b)^2,$$

$$F_1(a,b,t) = \frac{1}{a} + \frac{(a+b)^2}{b(2D_0vt)},$$

$$F_2(a,b,t) = \frac{(a-b)^2}{ab} + 1 + \frac{(a+b)^2}{2D_0vt},$$

$$F_3(a,b,t) = \frac{3}{a^2} + \frac{3(a+b)}{a(2D_0vt)} + \frac{(a+b)^3}{b(2D_0vt)^2},$$

$$F_4(a,b,t) = \left[\frac{3}{a^2} + \frac{(a+b)^2 g_3(a,b)}{ab^3(2D_0vt)} + \frac{(a+b)^4}{b^2(2D_0vt)^2}\right],$$

$$F_5(a,b,t) = \left[\frac{15}{a^3} + \frac{15(a+b)}{a^2(2D_0vt)} - \frac{(a+b)^3(3ab - 6b^2 - a^2)}{ab^3(2D_0vt)^2} + \frac{(a+b)^5}{b^2(2D_0vt)^3}\right].$$

*(a) First-order contributions.* The first order absorption and scattering corrections to the transmitted photon flux density were reported previously [14–16,18]. For absorption, the corresponding photon densities are given by

$$I_{n,k_{abs}}^{\alpha\beta(1)}(\vec{r}_{\det},t) = \frac{-\delta\mu_a \exp(-\mu_{a0}vt)}{4\pi D_0(4\pi D_0vt)^{3/2}} \int_V \frac{r_n^\alpha + r_{pk}^\beta}{r_n^\alpha r_{pk}^\beta}$$

$$\times \exp\left[-\frac{(r_n^\alpha + r_{pk}^\beta)^2}{4D_0vt}\right]dV_p \qquad (A1)$$

and for scattering by

$$I_{n,k_{scat}}^{\alpha\beta(1)}(\vec{r}_{\det},t) = \frac{\delta D \exp(-\mu_{a0}vt)}{2D_0(4\pi D_0vt)^{5/2}}$$

$$\times \int_V \{(\vec{r}_n^{*\alpha} \cdot \vec{r}_{pk}^\beta)g_2(r_n^\alpha, r_{pk}^\beta)F_2(r_n^\alpha, r_{pk}^\beta, t)\}$$

$$\times \exp\left[-\frac{(r_n^\alpha + r_{pk}^\beta)^2}{4D_0vt}\right]dV_p. \qquad (A2)$$

*(b) Second-order expressions.* Second-order absorption and scattering corrections to the transmitted photon flux density were reported previously [24]. The corresponding photon density for second-order absorption correction is derived from

$$I_{m,n,k_{abs-abs}}^{\alpha\beta\gamma(2)}(\vec{r}_{\det},t) = \frac{(\delta\mu_a)^2 \exp(-\mu_{a0}vt)}{(4\pi D_0)^2(4\pi D_0vt)^{3/2}} \int_V \int_V \frac{r_{pqm}}{r_m^\alpha r_{pn}^\beta r_{qk}^\gamma}$$

$$\times \exp\left[-\frac{r_{pqm}^2}{4D_0vt}\right]dV_p dV_q, \qquad (A3)$$

and the absorption-scattering cross term from

$$I_{m,n,k_{abs-scat}}^{\alpha\beta\gamma(2)}(\vec{r}_{\det},t) = \frac{-\delta\mu_a \delta D \exp(-\mu_{a0}vt)}{(4\pi D_0)^2(4\pi D_0vt)^{3/2}}$$

$$\times \int_V \int_V \frac{(\vec{r}_{pn}^{*\beta} \cdot \vec{r}_{qk}^\gamma)}{(r_{pn}^\beta)^2(r_{qk}^\gamma)^2}H_1(t)$$

$$\times \exp\left[-\frac{r_{pqm}^2}{4D_0vt}\right]dV_p dV_q, \qquad (A4)$$

where

$$H_1(t) = \frac{1}{r_{pq}^+}g_1(r_{pn}^\beta, r_{qk}^\gamma)F_1(r_{pq}^+, r_m^\alpha, t) + F_3(r_{pq}^+, r_m^\alpha, t).$$

The scattering-absorption cross term is given by

$$I_{m,n,k_{scat-abs}}^{\alpha\beta\gamma(2)}(\vec{r}_{\det},t) = \frac{-\delta\mu_a \delta D \exp(-\mu_{a0}vt)}{(4\pi D_0)^2(4\pi D_0vt)^{3/2}}$$

$$\times \int_V \int_V \frac{(\vec{r}_m^{*\alpha} \cdot \vec{r}_{pn}^\beta)}{(r_{pn}^\beta)^3 r_{qk}^\gamma}H_2(t)$$

$$\times \exp\left[-\frac{r_{pqm}^2}{4D_0vt}\right]dV_p dV_q, \qquad (A5)$$

where

$$H_2(t) = \frac{r_{qk}^\gamma}{(r_m^\alpha)^2}F_1(r_m^\alpha, r_{pq}^+, t) + \frac{r_{pn}^\beta(r_{pq}^+)^2}{2D_0vt}g_2(r_m^\alpha, r_{pq}^+)F_2(r_m^\alpha, r_{pq}^+, t),$$

and second-order scattering contributions are calculated using

$$I_{m,n,k_{scat-scat}}^{\alpha\beta\gamma(2)}(\vec{r}_{\det},t) = \frac{-(\delta D)^2 \exp(-\mu_{a0}vt)}{8\pi(D_0)^2(4\pi D_0vt)^{5/2}}$$

$$\times \int_V \int_V \left[\frac{\vec{\vec{r}}_{qm}^{**}H_3(t)}{(r_{pn}^\beta)^2(r_{qk}^\gamma)^2} - \frac{\vec{r}_{pm}^*\vec{r}_{pq}^*H_4(t)}{(r_{pn}^\beta)^3}\right]$$

$$\times \exp\left[-\frac{r_{pqm}^2}{4D_0vt}\right]dV_p dV_q, \qquad (A6)$$

where

$$H_3(t) = \frac{r_{pqm}}{(r_m^\alpha)^2 r_{pq}^+}g_1(r_{pn}^\beta, r_{qk}^\gamma)F_2(r_m^\alpha, r_{pq}^+, t) + F_4(r_{pq}^+, r_m^\alpha, t),$$

$$H_4(t) = \frac{3g_2(r_m^\alpha, r_{pq}^+)}{(r_{pn}^\beta)^2}F_2(r_m^\alpha, r_{pq}^+, t) + \frac{g_3(r_{pn}^\beta, r_{qk}^\gamma)}{r_{pq}^+ r_{pn}^\beta(r_{qk}^\gamma)^3}F_4(r_{pq}^+, r_m^\alpha, t)$$

$$+ \frac{1}{(r_{qk}^\gamma)^2}F_5(r_{pq}^+, r_m^\alpha, t).$$

*(c) Integrability of second-order contributions at $\vec{r}_p = \vec{r}_q$.* The double volume integrals appearing in Eqs. (A3)–(A6) are taken over all locations $\vec{r}_p, \vec{r}_q$ within the heterogeneity of volume $V$. As can be seen from Eq. (A6) the two terms of the integrand within the brackets contain contributions proportional to $(r_{pn}^\beta)^{-3}$. For $n=\beta=0$, $r_{pn}^\beta = |\vec{r}_p - \vec{r}_q|$ and, therefore, $r_{pn}^\beta = 0$ when the two position vectors $\vec{r}_p, \vec{r}_q$ coincide. Here we briefly show that the innermost volume integral over the location $\vec{r}_q$ is integrable even in that case and does not lead a logarithmic singularity as reported recently [24]. To this end we select a small sphere of radius $\varepsilon$ (volume $V_\varepsilon$), centered at $\vec{r}_p$ and express the innermost integral of Eq. (A6) as

$$\text{Int} = \int_{V-V_\varepsilon}\left[\frac{\vec{\vec{r}}_{qm}^{**}H_3(t)}{(r_{pn}^\beta)^2(r_{qk}^\gamma)^2} - \frac{\vec{r}_{pm}^*\vec{r}_{pq}^*H_4(t)}{(r_{pn}^\beta)^3}\right]\exp\left[-\frac{r_{pqm}^2}{4D_0vt}\right]dV_q$$

$$+ g_2(r_m^\alpha, \tilde{r}_{pk}^\gamma)F_2(r_m^\alpha, \tilde{r}_{pk}^\gamma, t)\exp\left[-\frac{(r_m^\alpha + \tilde{r}_{pk}^\gamma)^2}{4D_0vt}\right]$$

$$\times \int_0^\varepsilon \frac{d\rho}{\rho}\vec{r}_m^{*\alpha}\left\{\int_0^\pi\int_0^{2\pi}\left(\hat{1} - \frac{3\vec{\rho}\vec{\rho}}{\rho^2}\right)\cdot\sin\vartheta d\vartheta d\varphi\right\}\cdot\vec{r}_{pk}^\gamma$$

$$+ \int_{V_\varepsilon}O([r_{pn}^\beta]^\ell)dV_q, \qquad (A7)$$

where $\tilde{r}_{pk}^\gamma = \vec{r}_p - \vec{R}_{0k}^\gamma$, $\vec{\rho} = \vec{r}_q - \vec{r}_p$, $\hat{1}$ is the unit tensor and $O([r_{pn}^\beta]^\ell)$ contains expressions $|\vec{r}_p - \vec{r}_q|^\ell$ with $\ell \geq -2$, making the last integral integrable. The second rank tensor $\hat{1} - \frac{3\vec{\rho}\vec{\rho}}{\rho^2}$ is traceless and symmetric, the average of which vanishes when taken over the unit sphere. Therefore, the second summand of Eq. (A7) is identically zero and the innermost integral of Eq. (A6) is integrable. Likewise, as can be seen from Eq. (A3), the integrand of the pure absorption term is proportional to $|\vec{r}_p - \vec{r}_q|^{-1}$, whereas the integrand of the absorption-scattering [see Eq. (A4)] and scattering-absorption [Eq. (A5)] contributions contains $|\vec{r}_p - \vec{r}_q|^{-2}$ in lowest order, making all double volume integrals integrable.

*(d) Approximate scaling properties of transmitted photon densities and shape functions.* It follows from Eqs. (A1) and

([A2](#)) that the expressions $D_0 \exp(+\mu_{a0}vt)I^{(1)}_{abs}(\vec{r}_{det},t)/\delta\mu_a$ and $D_0 \exp(+\mu_{a0}vt)I^{(1)}_{scat}(\vec{r}_{det},t)/\delta D$ do not explicitly depend on the background optical properties $\mu_{a0}, D_0$, apart from the small displacement of the photon source into the medium at $\vec{r}_0 = (0,0,1/\mu'_{s0})$ and the small shift of the boundaries to $z=-z_e$, $z=d+z_e$, but on the scaled time variable $\tau=2D_0vt$ only. Likewise, the same holds true for the expressions $D_0^2\exp(+\mu_{a0}vt)I^{(2)}_{abs\text{-}abs}(\vec{r}_{det},t)/(\delta\mu_a)^2$, $D_0^2\exp(+\mu_{a0}vt)I^{(2)}_{abs\text{-}scat}(\vec{r}_{det},t)\delta\mu_a\delta D$, $D_0^2 \exp(+\mu_{a0}vt)$ $\times I^{(2)}_{scat\text{-}abs}(\vec{r}_{det},t)/\delta\mu_a\delta D$, and $D_0^2 \exp(+\mu_{a0}vt)I^{(2)}_{scat\text{-}scat}$ $\times(\vec{r}_{det},t)/(\delta D)^2$, as can be seen from Eqs. ([A3](#))–([A6](#)). Therefore, when changing background optical properties but keeping the overall geometry unchanged these expressions or the modified shape functions $g^{(1)}(\tau)$, $g^{(2)}(\tau)$ defined as

$$g^{(1)}(\tau) = \exp(+\mu_{a0}vt)f^{(1)}(t), \tag{A8}$$

$$g^{(2)}(\tau) = D_0 \exp(+\mu_{a0}vt)f^{(2)}(t) \tag{A9}$$

[cf. Eqs. ([6](#))–([11](#))] can be obtained to good approximation simply by rescaling, allowing to readily calculate the contributions $I^{(1)}(\vec{r}_{det},t)$, $I^{(2)}(\vec{r}_{det},t)$, as well as the shape functions $f^{(1)}(\vec{r}_{det},t)$, $f^{(2)}(\vec{r}_{det},t)$.

## APPENDIX B

In this appendix we derive the Cauchy criterion for the convergence of the Born series of a pure absorbing heterogeneity of arbitrary shape, starting from Eq. ([16](#)). To this end we assume that one can enclose the volume $V$ of the heterogeneity within a sphere $S$, which lies entirely inside the slab. The radius of this sphere is denoted by $R_{imp}$ and its center is located at $\vec{r}_{imp}$. In addition we consider only the dominant term in Eq. ([16](#)) for which $m_p=0$ and $\alpha_p=0$ (positive source), because the sum over mirror images is known to converge rapidly [33]. The sum in the numerator in Eq. ([16](#)) represents the length of the interaction path; an upper limit is given by $L^{(N)}=2NR_{imp}+|\vec{r}_{det}-\vec{r}_{imp}|+|\vec{r}_0-\vec{r}_{imp}|$. The exponential functions appearing in Eq. ([16](#)) are always smaller than unity, so that one obtains

$$|I^{\alpha_0,\ldots,\alpha_N \,(N)}_{m_0,\ldots,m_N}| \leq \frac{e^{-\mu_a vt}}{(4\pi D_0 vt)^{3/2}} \left(\frac{|\delta\mu_a|}{4\pi D_0}\right)^N \frac{L^{(N)}}{|\vec{r}_{imp}-\vec{r}_{det}|-R_{imp}}$$

$$\times \int_S \left(\frac{dV_1}{r^+_{0,0}} \int_S \left\{\frac{dV_2}{r^+_{1,0}} \cdots \int_S \left[\frac{dV_{N-1}}{r^+_{N-2,0}}\right.\right.$$

$$\left.\left.\times \int_S \left(\frac{dV_N}{r^+_{N-1,0}}\right)\right] \cdots \right\}\right). \tag{B1}$$

Here we used the fact that the sphere lies inside the slab allowing us to estimate the lower limit for $r^+_{N,0}$ as $|\vec{r}_{imp}-\vec{r}_{det}|-R_{imp}>0$. To estimate the integrals over the singularities, we consider the innermost integral first,

$$I = \int_S \frac{dV_N}{|\vec{r}_N - \vec{r}_{N-1}|}. \tag{B2}$$

We compare this integral with that over a sphere $\widetilde{S}$ with the same radius $R_{imp}$ but centered at $\vec{r}_{N-1}$ rather than at $\vec{r}_{imp}$,

$$\widetilde{I} = \int_{\widetilde{S}} \frac{dV_N}{|\vec{r}_N - \vec{r}_{N-1}|}. \tag{B3}$$

The overlap region of $S$ and $\widetilde{S}$ contributes equally to both integrals. The two remaining regions have the same volume and shape. However, the integrand in Eq. ([B2](#)) is smaller than $1/R_{imp}$, whereas the opposite holds true for the integrand in Eq. ([B3](#)) and, therefore, $I \leq \widetilde{I}$. By elementary integration one finds $\widetilde{I}=2\pi R_{imp}^2$. This upper limit no longer depends on $\vec{r}_{N-1}$, and the same procedure can be repeated to find upper limits for all integrals in Eq. ([B1](#)), yielding

$$|I^{\alpha_0,\ldots,\alpha_N \,(N)}_{m_0,\ldots,m_N}| \leq \frac{e^{-\mu_a vt}}{(4\pi D_0 vt)^{3/2}} \left(\frac{|\delta\mu_a|}{4\pi D_0}\right)^N$$

$$\times \frac{2NR_{imp}+|\vec{r}_{det}-\vec{r}_{imp}|+|\vec{r}_0-\vec{r}_{imp}|}{|\vec{r}_{imp}-\vec{r}_{det}|-R_{imp}}(2\pi R_{imp}^2)^N. \tag{B4}$$

Since terms of power $N$ prevail over linear terms, we obtain as Cauchy criterion for the convergence of the Born series of a pure absorbing heterogeneity the expression given in Eq. ([17](#)).

[1] M. A. Franceschini, K. T. Moesta, S. Fantini, G. Gaida, E. Gratton, H. Jess, W. W. Mantulin, M. Seeber, P. M. Schlag, and M. Kaschke, Proc. Natl. Acad. Sci. U.S.A. **94**, 6468 (1997).

[2] L. Götz, S. H. Heywang-Köbrunner, O. Schütz, and H. Siebold, Aktuelle Radiol. **8**, 31 (1998).

[3] S. B. Colak, M. B. van der Mark, G. W. 't Hooft, J. H. Hoogenraad, E. S. van der Linden, and F. A. Kuijpers, IEEE J. Sel. Top. Quantum Electron. **5**, 1143 (1999).

[4] J. P. Culver, R. Choe, M. J. Holboke, L. Zubkov, T. Durduran, A. Slemp, V. Ntziachristos, B. Chance, and A. G. Yodh, Med.

Phys. **30**, 235 (2003).

[5] H. Dehghani, B. W. Pogue, S. P. Poplack, and K. D. Paulsen, Appl. Opt. **42**, 135 (2003).

[6] D. Grosenick, K. T. Moesta, M. Möller, J. Mucke, H. Wabnitz, B. Gebauer, C. Stroszczynski, B. Wassermann, P. M. Schlag, and H. Rinneberg, Phys. Med. Biol. **50**, 2429 (2005).

[7] P. Taroni, A. Torricelli, L. Spinelli, A. Pifferi, F. Arpaia, G. Danesini, and R. Cubeddu, Phys. Med. Biol. **50**, 2469 (2005).

[8] T. Yates, J. C. Hebden, A. Gibson, N. Everdell, S. R. Arridge, and M. Douek, Phys. Med. Biol. **50**, 2503 (2005).

[9] D. B. Jakubowski, A. E. Cerussi, F. Bevilacqua, N. Shah, D.

Hsiang, J. Butler, and B. J. Tromberg, J. Biomed. Opt. **9**, 230 (2004).

[10] D. Grosenick, H. Wabnitz, K. T. Moesta, J. Mucke, M. Möller, C. Stroszcynski, J. Stößel, B. Wassermann, P. M. Schlag, and H. H. Rinneberg, Phys. Med. Biol. **49**, 1165 (2004).

[11] P. Taroni, G. Danesini, A. Torricelli, A. Pifferi, L. Spinelli, and R. Cubeddu, J. Biomed. Opt. **9**, 464 (2004).

[12] B. W. Pogue, S. Jiang, H. Dehghani, C. Kogel, S. Soho, S. Srinivasan, X. Song, T. D. Tosteson, S. P. Poplack, and K. D. Paulsen, J. Biomed. Opt. **9**, 541 (2004).

[13] D. Grosenick, H. Wabnitz, H. H. Rinneberg, K. T. Moesta, and P. M. Schlag, Appl. Opt. **38**, 2027 (1999).

[14] S. R. Arridge, Appl. Opt. **34**, 7395 (1995).

[15] J. C. Hebden and S. R. Arridge, Appl. Opt. **35**, 6788 (1996).

[16] S. Carraresi, T. S. M. Shatir, F. Martelli, and G. Zaccanti, Appl. Opt. **40**, 4622 (2001).

[17] M. R. Ostermeyer and S. L. Jacques, J. Opt. Soc. Am. A **14**, 255 (1997).

[18] M. Morin, S. Verreault, A. Mailloux, J. Frechette, S. Chatingy, Y. Painchaud, and P. Beaudry, Appl. Opt. **39**, 2840 (2000).

[19] M. Morin, S. Chatingy, A. Mailloux, Y. Painchaud, and P. Beaudry, Proc. SPIE **3597**, 67 (1999).

[20] B. Wassermann, A. Kummrow, K. T. Moesta, D. Grosenick, J. Mucke, H. Wabnitz, M. Möller, R. Macdonald, P. M. Schlag, and H. Rinneberg, Opt. Express **13**, 8571 (2005).

[21] S. R. Arridge, P. van der Zee, M. Cope, and D. T. Delpy, Proc. SPIE **1431**, 204 (1991).

[22] A. Torricelli, L. Spinelli, A. Pifferi, P. Taroni, and R. Cubeddu, Opt. Express **11**, 853 (2003).

[23] L. Spinelli, A. Torricelli, A. Pifferi, P. Taroni, and R. Cubeddu, Appl. Opt. **42**, 3145 (2003).

[24] B. Wassermann, Phys. Rev. E **74**, 031908 (2006).

[25] M. A. O'Leary, D. A. Boas, B. Chance, and A. G. Yodh, Phys.

[26] D. A. Boas, M. A. O'Leary, B. Chance, and A. G. Yodh, Proc. Natl. Acad. Sci. U.S.A. **91**, 4887 (1994).

Rev. Lett. **69**, 2658 (1992).

[27] X. D. Li, T. Durduran, A. G. Yodh, B. Chance, and D. N. Pattanayak, Opt. Lett. **22**, 573 (1997).

[28] X. Li, D. N. Pattanayak, T. Durduran, J. P. Culver, B. Chance, and A. G. Yodh, Phys. Rev. E **61**, 4295 (2000).

[29] D. Grosenick, H. Wabnitz, K. T. Moesta, J. Mucke, P. M. Schlag, and H. Rinneberg, Phys. Med. Biol. **50**, 2451 (2005).

[30] V. Tuchin, *Tissue Optics Light Scattering Methods and Instruments for Medical Diagnostics* (SPIE, Bellingham, 2000), pp. 6–11.

[31] M. Bassani, F. Martelli, G. Zaccanti, and D. Contini, Opt. Lett. **22**, 853 (1997).

[32] R. Pierrat, J.-J. Greffet, and R. Carminati, J. Opt. Soc. Am. A **23**, 1106 (2006).

[33] M. S. Patterson, B. Chance, and B. C. Wilson, Appl. Opt. **28**, 2331 (1989).

[34] D. Contini, F. Martelli, and G. Zaccanti, Appl. Opt. **36**, 4587 (1997).

[35] G. Arfken, *Mathematical Methods for Physicists* (Academic Press, New York, 1970), p. 738.

[36] M. Schweiger, and S. R. Arridge, http://www.medphys.ucl.ac.uk/~martins/toast/index.html

[37] S. R. Arridge, M. Schweiger, M. Hiraoka, and D. T. Delpy, Med. Phys. **20**, 299 (1993).

[38] D. Grosenick, B. Wassermann, R. Macdonald, H. Rinneberg, A. Torricelli, L. Spinelli, and R. Cubeddu, Proc. SPIE **5859**, 89 (2005).

[39] R. L. P. Van Veen, H. J. C. M. Sterenborg, A. W. K. S. Marinelli, and M. Menke-Pluymers, J. Biomed. Opt. **9**, 1129 (2004).